MASTERARBEIT | MASTER'S THESIS

Titel | Title

A Lagrangian approach for quantifying the impact of space debris on the atmosphere

verfasst von | submitted by

Francesca Carmela Papatola BSc

angestrebter akademischer Grad | in partial fulfilment of the requirements for the degree of

Master of Science (MSc)

Wien | Vienna, 2026

Studienkennzahl lt. Studienblatt | Degree programme code as it appears on the student record sheet:	UA 066 614
Studienrichtung lt. Studienblatt | Degree programme as it appears on the student record sheet:	Masterstudium Meteorology and Climate Science
Betreut von | Supervisor:	Univ.-Prof. Mag. Dr. Andreas Stohl
Mitbetreut von | Co-Supervisor:	Dr. Marina Dütsch BSc ETH MSc ETH

Abstract

Due to the growing activities in the space sector the number of reentering human-made objects into the atmosphere has seen an increase since the year 2020. Especially since metals from spacecraft were found in Arctic aerosol measurements, this topic has gained attention. This work focuses on quantifying the impact of space debris emissions on the atmosphere, by employing a Lagrangian particle dispersion model. Alumina and nitrogen oxides emissions are studied due to their impact on ozone depletion, cloud nucleation, and radiative forcing. It is of interest to quantify their atmospheric lifetimes, zonal and vertical dispersion, as well as the influence of particle size and reentry location on these processes.

A statistically representative, one-year reentry inventory is created based on the reentry activities of the years 2021 to 2025. The dispersion of these emissions in the atmosphere is then simulated for a 6-year time horizon. The reentry trajectories of individual satellites are simulated, along which emissions are determined for each reentry object over the altitude range from 90 to 20 km. A sensitivity study is performed to evaluate the impact of the assumed diameter of the alumina particles on the transport and deposition pattern. Particles with a diameter of 100 nm, 50 nm, and smaller than 1 nm are modelled, along with NO_x emissions.

Results indicate that the transport is highly influenced by the Brewer-Dobson circulation, leading to high mass mixing ratios in the polar stratosphere. Alumina particles show a shorter atmospheric lifetime of 1.5 years than NO_x with about 2 years. It is found that, in later model years, smaller particle diameters lead to higher mass mixing ratios than larger particle diameters. During transport, filamentous structures and sharp gradients develop in the emission fields. This indicates that a Lagrangian modelling approach can improve the understanding of transport pathways and structures of space-debris emissions.

Kurzfassung

Aufgrund der zunehmenden Aktivität im Weltraumsektor steigt die Zahl der in die Atmosphäre wieder eintretenden, menschengemachten Objekte seit dem Jahr 2020 stetig an. Insbesondere, seitdem in Aerosolmessungen in der Arktis Metalle aus Raumfahrzeugen nachgewiesen werden konnten, hat dieses Thema an Aufmerksamkeit gewonnen. Diese Arbeit konzentriert sich auf die Quantifizierung der Auswirkungen von Emissionen wiedereintretender Raumfahrzeuge auf die Atmosphäre unter Verwendung eines Lagrange'schen Partikeldispersionsmodells. Aluminiumoxid- und Stickoxidemissionen werden aufgrund ihrer Auswirkungen auf den Ozonabbau, die Wolkenkeimbildung und den Strahlungsantrieb untersucht. Von Interesse ist ihre atmosphärische Lebensdauer, zonale und vertikale Ausbreitung sowie der Einfluss von Partikelgröße und Wiedereintrittsort auf diese Prozesse.

Auf der Grundlage der Wiedereintrittsaktivitäten der Jahre 2021 bis 2025 wird ein statistisch repräsentatives Wiedereintrittsinventar für ein Jahr erstellt. Die Ausbreitung dieser Emissionen in der Atmosphäre wird anschließend über einen Zeitraum von sechs Jahren simuliert. Es werden die Wiedereintrittsbahnen einzelner Satelliten simuliert, entlang derer die Emissionen für jedes Wiedereintrittsobjekt im Höhenbereich von 90 bis 20 km bestimmt werden. Zur Bewertung des Einflusses des angenommenen Durchmessers der Aluminiumoxidpartikel auf das Transport- und Ablagerungsmuster wird eine Sensitivitätsstudie durchgeführt. Partikel mit einem Durchmesser von 100 nm, 50 nm und kleiner als 1 nm werden zusammen mit NO_x-Emissionen modelliert.

Die Ergebnisse zeigen, dass der Transport stark von der Brewer-Dobson-Zirkulation beeinflusst wird, was zu hohen Massenmischungsverhältnissen in der polaren Stratosphäre führt. Aluminiumoxidpartikel weisen mit 1,5 Jahren eine kürzere atmosphärische Lebensdauer auf als NO_x mit etwa 2 Jahren. Es zeigt sich, dass in späteren Modelljahren Partikel mit kleinerem Durchmesser zu höheren Massenmischungsverhältnissen führen als Partikel mit größerem Durchmesser. Während des Transports entwickeln sich in den Emissionsfeldern filamentartige Strukturen und starke Gradienten. Dies deutet darauf hin, dass eine Lagrange-Modellierung das Verständnis der Transportwege und Strukturen von Emissionen wiedereintretender Raumfahrzeuge verbessern kann.

Acknowledgements

I would like to acknowledge the efforts involved in providing spacecraft reentry data through Space-Track.org, operated by the United States Space Force; the DISCOSweb database and its APIs, operated by European Space Agency; and Jonathan's Space Report, maintained by Jonathan C. McDowell. Their continued efforts in making these datasets publicly accessible have been essential to this work. To translate the abstract from Englisch to German, as well as for checking spelling and grammar, the machine-learning-based language assistant DeepL (deepl.com), was used.

Further, I would like to thank Andreas Stohl not only for his supervision and advice, but also for introducing me to such a fascinating topic and giving me the opportunity to pursue my own research in this field. I would also like to thank Marina Dütsch for her support and for providing some incredibly useful pieces of code.
On a personal note, I would like to thank all the wonderful people in my life who have shown continuous support and encouragement throughout this journey. A special thanks goes to my parents for their unwavering support.

Contents

Abstract i

Kurzfassung ii

Acknowledgements iii

List of Tables vi

List of Figures vii

List of Algorithms 1

1. Introduction 1
- 1.1. Effects of ablation products in the atmosphere . . . 1
  - 1.1.1. Direct radiative forcing . . . 2
  - 1.1.2. Ozone depletion . . . 2
  - 1.1.3. Clouds . . . 2
  - 1.1.4. Nox . . . 3
- 1.2. Atmospheric transport modelling of space debris . . . 3
- 1.3. Research goals . . . 4

2. Theory and Methods 5
- 2.1. Reentry locations, mass and time . . . 6
- 2.2. Reentry trajectory model . . . 11
  - 2.2.1. GMAT's force model . . . 11
- 2.3. Emission profile . . . 13
- 2.4. FLEXPART . . . 17
  - 2.4.1. FLEXPART set up . . . 20

3. Results and Discussion 23
- 3.1. Alumina . . . 23
- 3.2. Transport and seasonality . . . 23
  - 3.2.1. Deposition . . . 30
  - 3.2.2. Size sensitivity . . . 33
- 3.3. NOx . . . 36
- 3.4. Limitations of the present method . . . 38

4. Conclusion 40

Bibliography **42**

A. Appendix **46**

List of Tables

2.1. Number of objects and total mass per mass category 10
2.2. Parameter values for the respective species files 22

3.1. Total mass per species that is either still suspended in the atmosphere (airborne), or deposited, as well as the sum of both, and the difference of the sum to the original released mass. The deviation between the sum of airborne and deposited mass to the total released mass is given in percentages in the same column. The difference indicates mass missing to the total emitted mass. All values are given in kg and for the end of the simulation. 31

List of Figures

2.1. Flowchart illustrating the workflow from satellite reentry data to reentry emissions, as input for the transport model. 6
2.2. Locations of the 120 km altitude points for 1143 sampled trajectories, displaying a representative year of reentries during the period of 2019 - 2025. 9
2.3. Mass histogram showing the number of reentered payload objects per mass bin from 2021 to 2025, and the by frequency of occurrence sampled subset of 1143 representative reentries. Original data from: DISCOSweb (ESA 2025a). . 10
2.4. Emissions of NO_x and aluminum adapted from Larson et al. (2017) and Bekki et al. (2021), respectively, and shown as mass fractions per 1-km bin as a function of altitude. 14
2.5. Example of the injected alumina mass as a fraction of satellite mass as a function of latitude, longitude and altitude, for the example of Starlink satellite 30046. Emissions are discretized to 397 release points, at which mass is injected into the atmosphere, for the purpose of atmospheric transport modelling. . . 15
2.6. Zonal mean of the alumina and NO_x emissions in the first model year, with a grid resolution of 1° meridional and 1 km vertical. 17

3.1. Zonal mean mass mixing ratio of alumina particles with a diameter of 50 nm. The left panel shows the six-year sum of January values, and the right panel shows the six-year sum of July values. Mass concentration is shown by the black contour lines in pg/m^3. 24
3.2. Mass mixing ratio of alumina particles with a diameter of 50 nm, at different altitudes, at the end of the first year of emissions. 25
3.3. Mass mixing ratio of the vertical distribution of the zonal mean of the alumina particles with a diameter of 50 nm in December for the time period of 2015-2020. Mass concentration is displayed by the black contour lines 26
3.4. Global average vertical mass concentration profiles, accumulated for the indicated timestamp and the corresponding dates from previous years. 27
3.5. Six-year sum of the zonal-mean mass mixing ratio of alumina particles with a diameter of 50 nm, for July. For each subplot, only reentries within the indicated region are considered: (a) tropics, (b) subtropics and mid-latitudes in the Southern Hemisphere, (c) subtropics and mid-latitudes in the Northern Hemisphere, (d) polar region of the Southern Hemisphere, and (e) polar region of the Northern Hemisphere. Each region is scaled by the fraction of total mass relative to the emitted mass in the respective region. Mass concentration is displayed by the black contour lines in pg/m^3. 29

3.6. Deposited mass as a function of time, shown in percentage of the total emitted mass. The total deposited mass is given as the sum of wet and dry deposition in the upper panel. The individual deposition modes are shown in the panel below. 30
3.7. Spatial distribution of deposited mass in ng/m^2 of particles with a diameter of 50 nm, at the end of the modelled period. 32
3.8. Percentage of wet deposition of the total deposition. Accumulated after 6-years of emission of particles with a diameter of 50 nm. 33
3.9. Zonal mean mass mixing ratio of the alumina tracer. The left panel shows the six-year sum of January values and the right panel shows the six-year sum of July values. Mass concentration is shown by the black contour lines in pg/m^3. 34
3.10. Zonal mean mass mixing ratio of alumina particles with a diameter of 100 nm. The left panel shows the six-year sum of January values, and the right panel shows the six-year sum of July values. Mass concentration is shown by the black contour lines in pg/m^3. 35
3.11. Zonal mean mass mixing ratio of NO$_x$. The left panel shows the six-year sum of January values, and the right panel shows the six-year sum of July values. Mass concentration is shown by the black contour lines in pg/m^3. 36
3.12. Mass mixing ratio of the vertical distribution of the zonal mean of the alumina particles with a diameter of NO$_x$ in December, for the time period of 2015-2020. Mass concentration is displayed by the black contour lines in pg/m^3. 37
3.13. Percentage of wet deposition of the total deposition. Accumulated after 6-years after emission for NO$_x$. 38

A.1. Reentry trajectory of the Starlink 30046 satellite, modelled with GMAT. The circle marks the end point of the trajectory, at an altitude of 20 km. Plot a) shows the ground track, and b) the altitude by elapsed time starting from 120 km. The x-axis starts at 800 min, since the trajectory needed to be propagated starting from the last sent TLE message, which was at a higher altitude. . . . 47
A.2. Example of the injected NO$_x$ mass as a fraction of satellite mass, as a function of latitude, longitude and altitude, for the example of Starlink satellite 30046. Emissions are discretized to 397 release points at which mass is injected into the atmosphere for the purpose of atmospheric transport modelling. 48
A.3. Mass mixing of the vertical distribution of the zonal mean of the alumina tracer particles in December of each year for the time period of 2015-2020. Mass concentration is displayed by the black contour lines in pg/m^3. 49
A.4. Mass mixing ratio of the vertical distribution of the zonal mean of the alumina particles with a diameter of 100 nm in December of each year, for the time period of 2015-2020. Mass concentration is displayed by the black contour lines in pg/m^3. 50

A.5. Six-year sum of the zonal-mean mass mixing ratio of alumina particles with a diameter of 50 nm, for January. For each subplot, only reentries within the indicated region are considered: (a) tropics, (b) subtropics and mid-latitudes in the Southern Hemisphere, (c) subtropics and mid-latitudes in the Northern Hemisphere, (d) polar region of the Southern Hemisphere, and (e) polar region of the Northern Hemisphere. Each region is scaled by the fraction of total mass relative to the emitted mass in the respective region. Mass concentration is displayed by the black contour lines in pg/m^3. 51
A.6. Vertical velocity from ERA5 as mean of June, July and August is shown in the left panel, and December, January and February in the right panel. A negative sign indicates upward motion, since this parameter is based on the Eta-coordinate system, where pressure decreases with increasing altitude. 52
A.7. Settling velocity for spherical alumina aerosols with a density of ρ_p = 3950 kg/m^3. 53
A.8. Spatial distribution of deposited mass in ng/m^2 of particles with a diameter of 100 nm at the end of the modelled period 53
A.9. Spatial distribution of deposited mass in ng/m^2 of alumina tracer particles at the end of the modelled period. 54
A.10. Spatial distribution of deposited mass in ng/m^2 of NO$_x$ at the end of the modelled period. 54
A.11. Percentage of wet deposition of the total deposition. Accumulated after 5-years after emission of particles with a diameter of 100 nm. 55
A.12. Percentage of wet deposition of the total deposition. Accumulated after 5-years after emission of particles, the alumina tracer. 55

1. Introduction

The increasing demand for satellite technology in different sectors, ranging from the growing commercialised space tourism and internet services, to military surveillance and research-focused Earth observation systems, is leading to an increase of objects in Earth's orbit (ESA 2025b). This development is favoured by the advancing space sector, which enables the launch of spacecraft at lower cost than ever before. Projections indicate additional 58,000 satellite launches until the end of the decade (United States Government Accountability Office 2022). Most of these are large satellite constellations that operate in a low Earth orbit (LEO) below 2000 km. This will lead to a four-fold increase compared to the 14,000 satellites that populate LEO in 2025 (ESA 2025b). LEO satellites have an average lifetime of 5 years at the end of which they are demised by decreasing orbital altitude to induce a controlled reentry (Maloney et al. 2025), a practice that has increased from 10 % to 60 % over the last decade (ESA 2024). The aim of a controlled reentry is the complete burn-up of the object in the atmosphere to minimize the risk of impact on the ground. This procedure is injecting emission of ablation products into all atmospheric layers. Estimations of mass influx due to anthropogenic reentering objects in 2024 range from 0.5 Gg (ESA 2025b) to 1.59 Gg (Schulz et al. 2025). The latter estimate includes information from multiple sources and files, therefore closing gaps which are present in the first estimate (Schulz et al. 2025). These values can be compared to the average meteoric mass influx, which is estimated to range from 5.4 Gg to 22.0 Gg per year (Carrillo-Sánchez et al. 2020, Hervig et al. 2022). While the estimate for the anthropogenic reentering mass is still smaller than the meteoric reentry mass, a continuous increase will add to the atmospheric burden. Considering future scenarios with an increase to values ranging from 2.7 to 8.1 Gg (Schulz et al. 2025) the anthropogenic mass influx will be of the same magnitude as the natural mass influx. Mapping the transport of emissions from spacecraft reentry in the atmosphere is a crucial part of understanding their environmental impact, and is the aim of this thesis.

1.1. Effects of ablation products in the atmosphere

During the demise process, the spacecraft enters the denser atmospheric layers around 120 km with high Mach number and hypersonic speed. The bluntness of the aircraft will create a bow shock wave. In the stagnation area behind the shock wave the flow becomes subsonic. The stagnation area is an area of high pressure and temperature. Surface temperature will rapidly increase to values between 1,700 K - 2,000 K (Ziniu et al. 2011, Park et al. 2017). In this environment atmospheric oxygen and nitrogen atoms will dissociate. In the boundary-layer, directly above the object's surface, the oxygen atoms will either recombine with nitrogen to NO_x or react with the metals from the spacecraft's surface. Aluminum makes up between 40 %

to 70 % of spacecrafts (Barker et al. 2024), which will vaporize and aerosolize at temperatures over 900 K (Greene et al. 2019). It can be considered that every aluminum atom oxidizes to alumina Al_2O_3 (Barker et al. 2024). These particles can have a diameter up to 10 nm, but might grow to diameters of d_p >100 nm due to secondary surface oxidation, mixing, and coagulation in the cold far-field reentry plume (Murphy et al. 2023). The main altitude breakup window for uncontrolled reentries is 80 km to 45 km (Bekki et al. 2021).

1.1.1. Direct radiative forcing

Alumina injection into the stratosphere is important due to its optical and chemical properties. Alumina has a complex refractive index of $\tilde{n}$=1.77+1.65 × 10^{-7}i and therefore has both scattering and absorbing properties (Dresselhaus et al. 2018). The exact impact of alumina aerosols has yet to be fully understood, but it can be stated that its refraction (n=1.77) is higher than its extinction ($\tilde{k} = 10^{-7}$), pointing towards a higher negative than positive forcing. Xu et al. (2024) reported a cooling of approximately -0.4 $\frac{W}{m^2}$ under an extreme geoengineering scenario with an atmospheric burden of 4 Tg. Ross and Sheafer (2014), on the other hand, found a net positive radiative forcing. Bekki et al. (2021) find no significant impact of alumina on radiative forcing. A recent study (Bernlochner et al. 2026) investigated the effect of the particle size on radiative forcing and showed a dependency of the sign and magnitude on particle diameter.

1.1.2. Ozone depletion

The even stronger climate impact of alumina is its potential to activate ozone depleting substances, like chlorine. Chlorine is present in the atmosphere in reservoir species (e.g., HCl, $ClONO_2$), which can release chlorine through heterogeneous nucleation on alumina particles. Chlorine will be photolyzed, resulting in activated chlorine radicals; these destroy ozone via a catalytic cycle. The induced ozone depletion by this process is an order of magnitude higher than for an equal mass of stratospheric sulfate aerosols (Jackman et al. 1998, Danilin et al. 2001).

1.1.3. Clouds

Alumina can be found in aqueous stratospheric sulfuric acid particles. These could act as ice nuclei for polar stratospheric and upper tropospheric cirrus clouds (Murphy et al. 2023). Cirrus clouds contribute to the uncertainties of climate forcing, and polar stratospheric clouds play a significant role in the ozone depletion at higher latitudes (Tritscher et al. 2021). Aerosols from spacecraft re-entering the atmosphere may act as ice nuclei in the lower mesosphere. Further statements on this issue cannot be made until more research has been carried out.

1.1.4. Nox

The NO_x reentry emission profile is narrower than that of alumina, producing the most NO_x between 80 km and 60 km. NO_x emissions can vary between 17.5 % to 100 % of mass, equivalent to the reentering object, depending on the method of reentry and approximation of NO_x production rate (Ryan et al. 2022). NO_x destroys ozone via a catalytic cycle (Larson et al. 2017). Ryan et al. (2022) found, for an economic optimistic scenario, 0.15 % ozone depletion in northern high latitude stratosphere due to a decade of NO_x emissions. Larson et al. (2017) estimated a loss of 0.5 % of the globally averaged ozone column.

1.2. Atmospheric transport modelling of space debris

To estimate the impact of aerosols from satellite reentries, it is important to understand how they are transported in the atmosphere. Since the main fraction of the ablated mass is released between 80 and 40 km, ranging from the mesosphere to stratosphere, multiple mechanisms influence the transport. The dominating transport patterns are uplift in the tropics, poleward transport in the stratosphere, and subsidence in the polar vortex. Transport from the stratosphere to the troposphere can be seen in tropopause folds. Tropopause folds are characterised by steep shear and temperature gradients around the jet stream core, creating intrusions from the stratosphere to the troposphere. The meridional mean mass transport in the stratosphere and lower mesosphere is dominated by the Brewer-Dobson circulations (BDC), transporting air towards the winter pole. The BDC has a deep-branch in the winter hemisphere that drives a poleward transport in the middle and upper stratosphere. Additionally, shallow-branches can be identified. These dominate in the lower stratosphere and upper troposphere, in both hemispheres. The shallow branches introduce a poleward flow as well, and are driven by Rossby-wave pumping. The mesosphere part of the circulation is driven by buoyancy or gravity waves. These introduce an eastward drag in the summer mesosphere and a westward drag in the winter hemisphere. These flows are then deflected by the Coriolis force, induced by the rotation of the Earth, and are redirected towards the equator or poles respectively. This drives a flow towards the winter pole, with subsidence over the winter pole and upward transport over the summer pole (Butchart 2014). The tropics are characterised by a strong upward transport and a lifted tropopause. In the Intertropical Convergence Zone, deep convection leads to a strong vertical uplift, classically associated with moist air masses. This produces a belt of precipitation in the subtropics, which acts as a removing process for atmospheric particles.
Taken together, air is lifted in the Tropics and then transported downward again in the middle and high latitudes by the BDC (Butchart 2014). The atmospheric transport behaviour depends on the lifetime of the particle in the atmospheric layer. In the mesosphere, particles with a longer lifetime and little gravitational settling will get transported to the winter pole by the Brewer-Dobson circulation and descend into the stratospheric polar vortex (Fisher et al. 1993). Plumb et al. (2002) showed that meteoric material can reach levels as low as 16 km due to diabatic subsidence of air masses by radiative cooling. Near the tropopause, particles will be

removed faster due to stratospheric tropospheric exchange processes (Deshler 2008). Particles with higher gravitational settling will settle more quickly and have a shorter lifetime. NO_x sees no gravitational settling and will therefore be transported to higher latitudes and stay in the upper stratosphere for longer.

Previous studies have run Eulerian global circulation models to improve the understanding of the interaction between these mechanisms and the ablation products of space debris. Murphy et al. (2023) did a 15-year simulation using the Whole Atmosphere Community Climate Model (WACCM6), releasing 0.4 Gg y^{-1} of Al_2O_3 between 60 km and 70 km in the 40°S to 80°S and 40°N to 80°N latitude bands. They found that concentrations of aerosols in the polar regions start to increase after a few months. Jain et al. (2023) used the specified chemistry version of WACCM (WACCM6-SC) and terrestrial mineral dust ($AlSiO_5$) as a proxy for alumina, and employing different model set ups for sensitivity studies, releasing 2.59 Gg y^{-1} to model released reentry mass. Similar approaches were conducted by Maloney et al. (2025), who coupled WACCM6 with the Community Aerosol and Radiation Model for Atmospheres (CARMA), releasing 10 Gg y^{-1} between 60 km and 70 km, and different cases for latitudinal distribution of emissions. Ryan et al. (2022) used the global GEOS-Chem CTM coupled to the Rapid Radiative Transfer Model for Global Climate to be able to include the impact on stratospheric O_3 depletion. To the best of the author's knowledge, no Lagrangian approach was pursued so far. In general, it is expected that the large scale transport patterns will look the same as seen in the extant literature, but Lagrangian transport models have some advantages compared to Eulerian models that could influence the results. When modelling the transport of aerosols, the mass will be conserved, making it ideal for particle transport, like alumina. No numerical diffusion occurs since Lagrangian models are numerically stable, which makes it possible to conserve sharp gradients. This is especially important for regions like the polar vortex, where sharp tracer gradients are present. It is to be expected that, looking at longer time horizons, filamentous structures will develop. The second advantage is that the model that will be used here runs on ERA5 re-analysis data, which will, especially in the stratosphere, result in more realistic results than free-running atmospheric simulations.

1.3. Research goals

The goal of this study is to identify the transport patterns of aerosols produced during the ablation of reentering spacecraft. Main objectives of this study are to quantify atmospheric lifetime of the ablation products and the main accumulation regions in the atmosphere, with respect to their zonal and vertical distribution. Furthermore, these aspects will be evaluated across different particle sizes and species, distinguishing between aerosol particles and gaseous species. Since Lagrangian transport models are able to preserve sharp gradients, the development of tracer gradients will also be investigated. In addition, it will be evaluated how the reentry location influences the transport pattern and final regions of deposition. A distinction will be made between wet and dry deposition. This is intended to demonstrate that a Lagrangian approach can yield meaningful results and help fill existing knowledge gaps in modelling the atmospheric fate of reentry products.

2. Theory and Methods

A key component of this work is the simulation of representative reentry events over a one-year period, assuming a reentry frequency that reflects the last five-year average reentry activity and an additional scenario representing enhanced future reentry activity. The complete workflow, from obtaining the trajectories of reentering satellites to the atmospheric transport model, is visualised in Figure 2.1 and is described as follows. To be able to make statements about a reentering satellite, four main components need to be known: orbital coordinates and mean motion parameters at an initial time step, as well as mass and drag area. Orbital coordinates and mean motion parameters can be retrieved from the Two-Line-Element (TLE) set decay messages from space-track.org (*Space-Track.org* 2026). Gravitational acceleration and drag play an important part in the reentering process. These forces depend on the mass and drag area of an object. The mass and drag area are retrieved from ESA's "Database and Information System Characterising Objects in Space" (DISCOS). These parameters are then used to initialize spacecraft trajectories in the General Mission Analysis Tool (GMAT), which are then propagated forward until the altitude reaches 20 km. The altitude of 20 km is chosen as a lower bound, as no burn-up of the satellites will occur below this altitude.

Since there is no database containing complete information on all reentering satellites, the global emission of debris will be modelled representatively. The reentry activity has been continuously changing in the last years (ESA 2025b), therefore the data relevant for the reentry trajectory calculations will be taken as a statistical representation of the last 5 years, from 2021 to 2025, to make sure to cover different reentry scenarios.

ESA classifies reentering objects into two main categories: Payload, i.e. objects that have no launch functionality, and Rocket Body, i.e. all objects with launch related functionality. Since the mechanism of ablation of rocket bodies is very different to that of payloads, due to their function and material composition, this work will only consider payload objects. The payload category is further extended by: Payload mission related objects, Payload fragmentation debris, and Payload debris. These three subcategories will be referred to as "Extended Payload Categories" in the following. The classification of "Payload" accounts for all operational satellites which are well tracked. All objects that are released from the main object, which can be intentional or due to a fragmentation event such as an explosion or collision belong to the extended Payload categories. These objects can vary highly in size, mass, and shape. The Payload class accounts for the main fraction of reentering mass. In 2025 only 1.4 % of the in DISCOSweb as Payload tracked mass belonged to the extended Payload (ESA 2025a). Therefore, in the following, only the main "Payload" category will be considered. According to ESA'S Annual Space Environment Report (ESA 2025b), in 2024, 1200 intact payload objects have reentered into Earth's atmosphere. In 2025, according to DISCOSweb (ESA 2025a), 1143 payload reentries and, according to Johnson's space catalogue (McDowell 2025), 1122 payload objects have reentered. DISCOSweb provides the longest and most consistent data set and

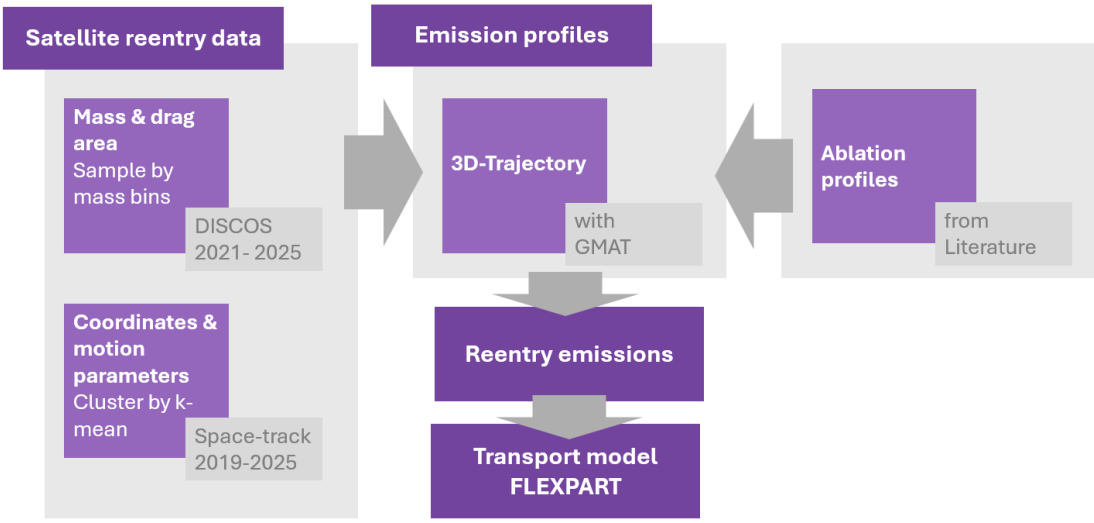

Figure 2.1.: Flowchart illustrating the workflow from satellite reentry data to reentry emissions, as input for the transport model.

was therefore used in the following.

Relative to the comparable steady reentry flux since the beginning of the space age a rapid increase in the number of reentering objects can be noted from 2021 to 2022. Since then, the number of reentering objects per year has fluctuated around 3-4 objects per day (ESA 2025b). This corresponds to 1095 - 1460 reentries per year. The number of 1143 payload objects that reentered in 2025 lies within this range.

2.1. Reentry locations, mass and time

A commonly used method of determining the position of an artificial satellite in Earth's orbit is by the propagation of TLE messages. TLE messages are published on the website space-track.org by the U.S. Department of Defense, for all tracked and unclassified objects in Earth's orbit. These messages are updated in regular intervals as long as an object is active. The TLE messages consist of two lines; the first line holds information such as:

- Satellite catalogue number
- Classification
- International designator
- First and second derivative of the mean motion
- Epoch: The time at which the orbital parameters are defined

- B* Drag Term: Measure for how much an object is affected by drag, according to its cross-sectional area, mass, coefficient of drag, and the atmospheric density, also referred to as ballistic coefficient.

And the second line:

- Orbital Inclination: The angle between the orbit of the satellite and the plane of reference.
- Right Ascension of the Ascending Node: Angle between a reference direction and the ascending node, the intersection of the reference plane with the orbit of the celestial body.
- Eccentricity: The deviation of an orbit from a circle.
- Argument of Perigee: The angle between ascending node and the nearest point of the satellite's orbit to Earth.
- Mean Anomaly: The fraction of orbit periods that have elapsed since the satellite has passed periapsis.
- Mean motion: The angular speed the satellite would need to have to complete one circular orbit in the same time as it takes for the elliptical orbit around Earth.

TLEs were originally developed for use together with Simplified General Perturbations (SGP) models based on the SGP-theory. Nowadays, the updated version SGP4 is used. This model can capture simplified drag, third body, and solar radiation pressure perturbations, as well as latitude-dependent deviations of Earth's gravitational field from spherical symmetry (Vallado et al. 2012). From these parameters, it is possible to propagate a satellite's orbital information forward in time. When using a SGP4 propagator, the BSTAR term plays the more important role; for an SPG propagator, the mean motion and its derivatives are used. Both parameters are used exclusively for one or the other theory. The elements in line 2 are mostly mean elements, calculated using the SGP4 orbital model (Kelso 2026).

A satellite is considered to have reentered once its altitude is lower than 100 km. This is known as the Kármán line. The last TLE message is, in most cases, created when the satellite is at an altitude between 180 - 140 km (Oliveira et al. 2025). Once the last TLE message is created, an object is considered "decayed" on space-track.org. To get a representative dataset of reentering satellites, all decayed satellites from 1 January 2019 - 1 January 2025 are queried from space-track.org. This gives a 6-year period of reentries, from which TLE messages are sampled to obtain a climatologically more representative set of reentry locations than for a single year. To obtain a distribution of possible reentry locations, TLE messages are grouped based on selected orbital parameters. Whilst orbital inclination has the highest impact on reentry latitude (Pardini et al. 2024), right ascension of the ascending node, eccentricity, argument of perigee, and mean motion were included to preserve correlations present in the original TLE population. The goal here was to get a sample distribution from a longer time period that represents real behaviour the closest, while covering all possible reentry locations.

To analyse the impact of global satellite reentries, it is important that the selected sample represents the full range of possible reentry locations and orbital behaviours. A purely random sampling approach was therefore considered insufficient, as less frequent orbital configurations and associated low-probability reentry regions could be underrepresented. Although such reentries occur less often, they may still become increasingly significant in the future, as the overall number of satellite reentries continues to rise. To address this, a clustering-based sampling approach was applied, using K-means.

This method is commonly used for grouping multidimensional datasets into subgroups, so-called clusters. For this, all parameters are projected into a feature space where their position is determined according to numerical value of the parameters. This can be multidimensional, enabling the analysis of the relationships of multiple parameters at once. This produces clusters of TLE messages that have similar orbital properties, making it possible to sample from each group. K-means clustering relies on the evaluation of the distance of each parameter in the feature space from a cluster centroid, the cluster mean. Clusters are created so that in-cluster variance will be minimised. In-cluster variance is calculated by the squared Euclidean distance, Eq. 2.1, where x and y are two points in an m-dimensional space of all available features: orbital inclination, right ascension of the ascending node, eccentricity, argument of perigee, and mean motion.

$$d(\mathbf{x}, \mathbf{y})^2 = \sum_{j=1}^{m} (x_j - y_j)^2 = \|\mathbf{x} - \mathbf{y}\|_2^2 \tag{2.1}$$

Since the parameters differ in their magnitudes and units, it is necessary to scale them to ensure comparability. To achieve this, all variables were standardized to a range of 0 to 1 by Min-Max normalization. This step prevents parameters with inherently larger numerical values from disproportionately influencing the clustering results. K-means then minimizes the within-cluster sum of squared errors, using the squared Euclidean distance between the centroid and a point x in the feature space (Raschka et al. 2022). This results in clusters of points that are close to one another in feature space, indicating that the corresponding orbital parameters are similar. The k-means method from the scikit-learn Python library provides all necessary functions to execute this method. The number of clusters, k, was set equal to the desired sample size (1143), such that each cluster contributes exactly one sample to the final dataset. After clustering, one TLE message was randomly selected from each cluster.

The date of reentry for each sampled satellite was acquired by shifting the object's reentry date to the year 2015, keeping month and day constant. Real-world reentries are equally distributed throughout the year, and this pattern was represented by this approach.

To be able to calculate the reentry trajectory, mass and drag area of an object need to be known. The mass and object area of reentering objects has changed towards higher object area and higher ratio of payloads to rocket bodies than before (ESA 2025b). To capture this in the mass and area data, only the period from 1 January 2021 and 1 January 2025 is taken into account. This data is taken from DISCOS, a database providing information about spacecraft for all trackable and unclassified objects, provided by ESA (2025a). This data was then sampled into bins by mass distribution. Loosely following taxonomy proposed by Botelho et al. (2019), payload objects are categorized into the following mass intervals: femto: 0-100 kg, mini:

100-500 kg, medium: 500-1000 kg, large: 1000-1500 kg and very large: >1500 kg. From this distribution, 1143 samples are taken, assigning them to the TLE messages aggregated before. Drag areas are kept associated to each item's mass, as in the DISCOS dataset.

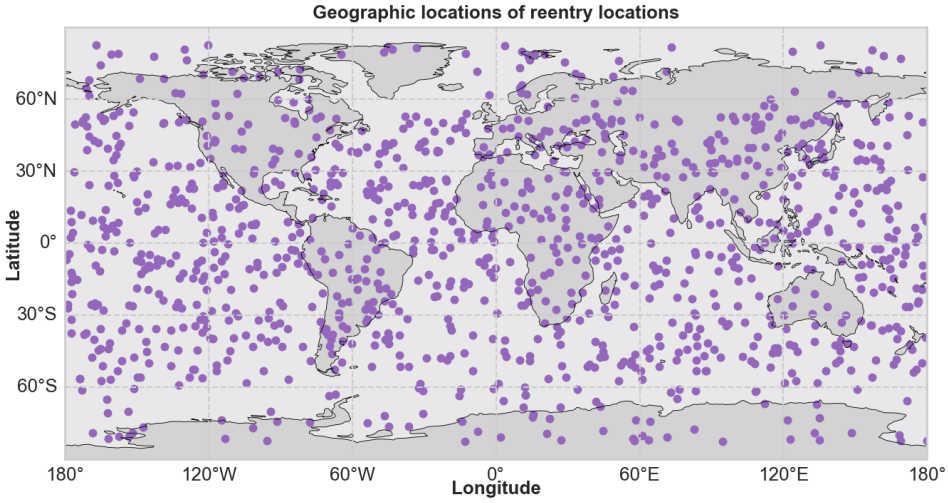

Figure 2.2.: Locations of the 120 km altitude points for 1143 sampled trajectories, displaying a representative year of reentries during the period of 2019 - 2025.

The mass and average cross section data was queried from DISCOSweb by getting all reentered objects, which were classified as payload. In the next step, the data points from the whole period were sorted into bins according to the mass categories described above. From this, 1143 data points were sampled randomly, according to the occurrence of mass in each bin. How the original distribution compares to the samples is shown in Figure 2.3.
The mass bins are composed as follows: femto: 631, mini: 400, medium: 65, large: 7, very large: 40. The total mass per category is shown in Table 2.1. The biggest contributions to total mass hold the categories mini and very large. Whilst satellites in the "mini" category have a lower mass, they have a high number of objects, on the contrary, the "very large" category only holds 40 objects, but their high individual mass makes them the largest share in the mass distribution. It can be noted that the "medium" category is dominated, with 55 out of 65, by objects with a mass of 730 kg. This corresponds to the Starlink satellite model v.2-mini with a dry mass of approximately 730 kg (Krebs 2026). The total mass of the 1143 sample satellites is 451,965 kg.

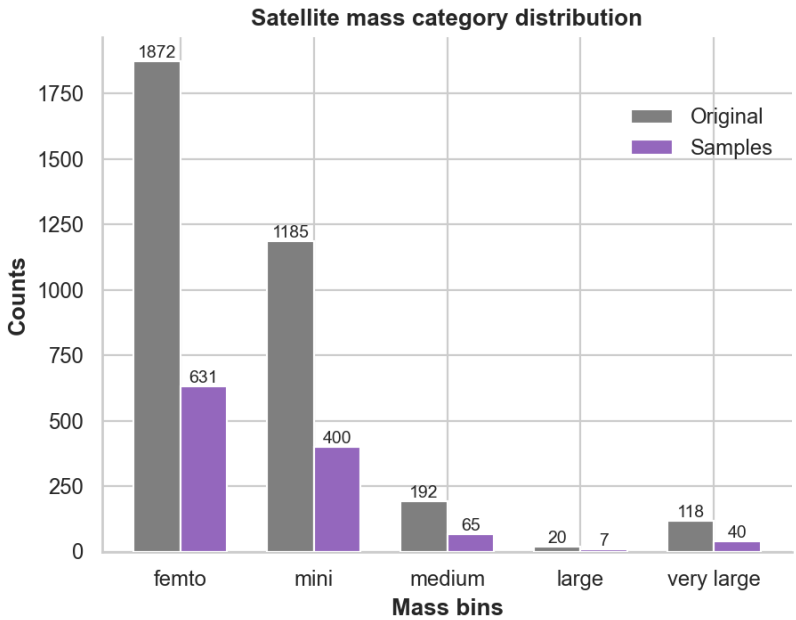

Figure 2.3.: Mass histogram showing the number of reentered payload objects per mass bin from 2021 to 2025, and the by frequency of occurrence sampled subset of 1143 representative reentries. Original data from: DISCOSweb (ESA 2025a).

Category	Number of objects	Mass [kg]	Average object mass [kg]
femto	631	6 218	10
mini	400	104 951	262
medium	65	46 457	712
large	7	8 891	1 270
very large	40	285 177	7 137
total	1143	451 695	

Table 2.1.: Number of objects and total mass per mass category

2.2. Reentry trajectory model

The sampled TLE messages then need to be propagated forward and used as initial conditions for modelling reentry trajectories. To achieve this, the GMAT model is used. GMAT is a tool by NASA designed to calculate trajectories of objects in orbits around astronomical space bodies (Jah et al. 2009). In a classical reentry analysis workflow, GMAT would be used to propagate TLE messages forward, and then use GMAT's output as input to the Object Reentry Survival Analysis Tool, also by NASA. The switch from GMAT to ORSAT is performed at the standard ORSAT entry altitude of 122 km (Ostrom et al. 2019). ESA has developed a comparable tool, Spacecraft Atmospheric Reentry and Aero-Thermal Break-up (SCARAB). Whilst SCARAB is a spacecraft oriented tool modelling spacecraft as realistically as possible to their real geometry, ORSAT is an object oriented tool which approximates spacecraft to their simplified geometric shapes, such as spheres, cylinders, etc. Both models vary in degrees of freedom and how aerodynamics, aerothermodynamics, and thermal analysis are implemented, but do give similar results (Kelley et al. 2010). Whilst reentry analysis tools model thermal breakup, ablation, and fragmentation, GMAT is more focused on spaceflight dynamics. To the author's knowledge, neither ORSAT nor SCARAB are available to the public. Therefore, in lack of an alternative, GMAT was used to get estimates of reentry trajectories in this work.
Since this work aims to model the distribution of reentry emissions in the atmosphere on long time scales and in a representative manner, these trajectories are assumed to be accurate enough estimations of the dispersion of emissions in Earth's atmosphere during reentry, even if individual accuracy of the trajectories is low.

2.2.1. GMAT's force model

The following paragraph discusses the fundamental equations used to describe the motion of a reentering spacecraft in GMAT as presented by Hughes (2007) and the GMAT user manual. All variables regarding the spacecraft are denoted by the subscript s. The central body of mass is Earth. GMAT models spacecraft motion as a function of the governing forces, which depend on the flight regime: gravity, spacecraft thrust, friction in the form of atmospheric drag, and solar radiation pressure. These are shown in their compact form in Eq.2.2.

$$\frac{d^2\mathbf{r}}{dt^2} = -\frac{\mu}{r^3}\mathbf{r} + \nabla\phi^{\circ}_{sj} + a_{3b} - \frac{1}{2}\frac{C_D A}{m_s}\rho\,\mathbf{v}^2_{\text{rel}}\hat{\mathbf{v}}_{\text{rel}} - P_{SR}\frac{C_R A_{\odot}}{m_s}\hat{r}_{s\odot} + a_{thrust} \tag{2.2}$$

In the first term, Earth's gravitational acceleration on an object is modelled by approximating Earth's mass as a simple point mass at a distance r. Here, μ is the product of G, the gravitational constant, and M, the central body's, in this case Earth's, mass. Due to its rotation, Earth is not a perfect sphere, but oblate, with an equatorial bulge. This deviation from spherical symmetry results in a non-uniform gravitational field that cannot be accurately represented by a simple point-mass model. To account for this deviation, the point-mass term is extended by spherical harmonic functions. Acceleration can be described as the gradient of the gravitational potential $\nabla\phi^{\circ}_{sj}$ of a spacecraft s at a point o in the gravitational field of a central

body, denoted by j. For non-spherical bodies, this can be expressed through the solution of the Laplace equation. In spherical coordinates, the Laplace equation is solved by the Legendre polynomials. In GMAT, the expression by Pines 1973 is used to avoid singularity at the poles. GMAT supports the option to consider n-body mass gravitational effects, captured in the a_{3b} term. However, these effects will not be the focus of this discussion, as re-entries occur in such close proximity to Earth that other gravitational effects become negligible.

Atmospheric drag is expressed through the fourth term in Eq.2.2. Drag acts in the opposite direction to the spacecraft's direction of motion. Drag depends strongly on the area that provides resistance to the atmosphere. This is not the object's entire surface, but only the portion projected onto a plane perpendicular to its direction of motion, commonly referred to as the drag reference area A. It is standard to set this equal to the mean cross-section of a spacecraft (Klinkrad et al. 1998). Furthermore, the velocity of the satellite relative to the reference frame of Earth's motion, the relative orbital velocity v_{rel} and the mass of the satellite m_s are taken into account. An important role as well plays the drag coefficient C_D, which depends on the geometry of the satellite. Usually, a drag coefficient of 2.2 is assumed for reentering satellites (Wang et al. 2024). Atmospheric drag, of course, varies highly with air density ρ. Since the density varies highly throughout the atmosphere, an atmospheric model is needed to capture these changes fully. GMAT provides multiple empirical atmospheric models. The Jacchia Roberts model, NASA's atmospheric model, the NRLMSISE-00 and its older version MSISE-90 (Picone et al. 2002). The Jacchia Roberts model is not defined below 100 km, and the NRLMSISE-00 is not available in the public release of GMAT. The 00 version mainly improved the thermosphere, and does not vary below 72.5 km from the 90 version, but this would still have been of interest to this study. Since it is not available, the next best option to use is the MSISE-90 version. MSISE models primarily define the temperature profile, and then derive pressure and density from it using hydrostatic equilibrium and the ideal gas law. Below ~300 km, this consistency breaks because temperature and atmospheric composition are fitted independently. To compensate for this, the model enforces an approximate hydrostatic equilibrium constraint in the 80–300 km region to maintain physical plausibility. In GMAT, MSISE-90 ranges from 0 to 1000 km.

The last two terms of Eq. 2.2, are not relevant for the present analysis. Whilst below 120 km, aerodynamic forces dominate, at higher altitudes, perturbations arise primarily from solar radiation pressure (SRP) (Klinkrad et al. 1998). This effect is caused by the momentum exchange during the impact of photons onto the spacecraft's surface, and depends on the reflectivity of the satellite's surface C_R, the area of the satellite's surface that is exposed to the Sun's radiation $A_\odot$, the Sun's radiation pressure, and the position of the spacecraft relative to the Sun. This effect can be neglected because it is marginal compared with the dominant aerodynamic and gravitational forces. The last term, a_{thrust}, accounts for spacecraft thrust. Since uncontrolled reentries are assumed, this term is not of interest.

To initialise the trajectories, the coordinates, as well as mean motion parameters from the sampled TLE's, are used to define the initial conditions of reentering spacecraft in GMAT. This is done alongside with the mass and average cross section data downloaded from DISCOSweb.

The average cross section is used as drag area. After sampling the TLE messages with k-mean clustering the positions of the satellites in Earth's orbit are calculated using the Python library SPG4 (Rhodes 2025). This library compiles the official C++ code from Revisiting Spacetrack Report 3 (AIAA 2006-6753) by Vallado et al. (2006). Since the SGP4 propagator returns Cartesian coordinates in a True Equator Mean Equinox (TEME) reference frame, they need to be transformed to Earth's Mean Equator and Mean Equinox (MEME). This is necessary, since GMAT works with a J2000 reference frame. Both of these are Earth centered inertial reference frames, but differ in how they define the equatorial plane and how they treat precession. To perform this, the Skyfield (Rhodes 2019) library can be used.

These parameters are then used to initialise spacecraft trajectories, determined by Eq. 2.2, in GMAT. This is then propagated forward using a RungeKutta89 propagator until the altitude reaches 20 km. The altitude of 20 km is chosen as lower bound, as the assumed total burnup of the satellites will have occurred at this stage. Runge–Kutta methods are one-step numerical methods for solving initial value problems for ordinary differential equations. In this implementation, an embedded Runge–Kutta method is used where two solutions of ninth and eighth order are computed in parallel. The difference between these solutions provides an estimate of the local truncation error. This error estimate is then used to adaptively adjust the step size, improving both accuracy and computational efficiency (Hughes 2007). GMAT then gives a latitude, longitude, altitude output by time step. The temporal resolution of the output lies within 0.1 to 5 seconds. An exemplary trajectory can be seen in Figure A.1. This shows the model trajectory output from the point when the satellite passed the 120 km upper boundary to the lower boundary of 20 km. Reentering satellites can cover thousands of kilometres during their descent. It is worth noting that the assumed trajectories here are overestimating the trajectory length. This is due to the model not considering break up processes, which would lead to fragmentation of the satellite into multiple smaller objects with perturbed trajectories, as well as the reduction of drag by the object becoming smaller as material is ablated.

2.3. Emission profile

NO_x is mainly produced from re-entry burn when the air surrounding the reentering spacecraft is heated behind the shock wave. This leads to dissociation of molecules that are already present in the atmosphere; oxygen and nitrogen will then recombine to nitric oxides. The emission of alumina, on the other hand, depends on the spacecraft surface reaching high enough temperatures for the aluminum to start evaporating. Bekki et al. (2021) modelled the mass loss fraction by altitude of a reentering spacecraft from 120 km to 0 km with SCARAB. This alumina profile is used as reference here. For the NO_x profile, the emission by altitude of the reentering Skylon rocket, modelled by Larson et al. (2017), will be used as reference. Since, for both publications, no datasets, but only the plots, are available, multiple points along the profiles were reconstructed by reading discrete points from the published plots. These points were subsequently interpolated using a skewed normal probability density function and fitted to the extracted data using nonlinear least-squares optimization from the Python scipy library. As expected, the aluminum profile in Figure 2.4 is slightly skewed towards higher altitudes. The NO_x profile shows a narrower emission region. The discrepancy between the two profiles

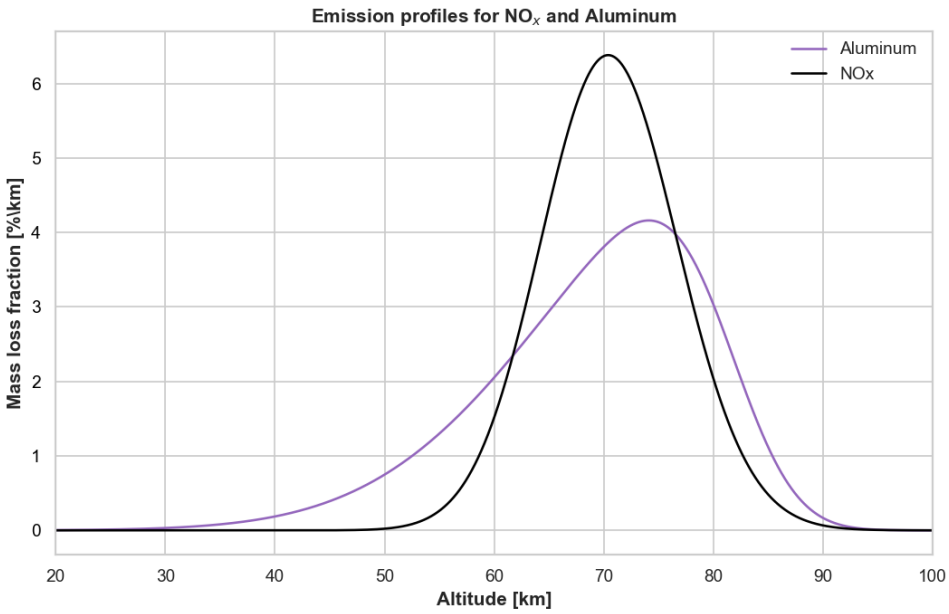

Figure 2.4.: Emissions of NO$_x$ and aluminum adapted from Larson et al. (2017) and Bekki et al. (2021), respectively, and shown as mass fractions per 1-km bin as a function of altitude.

may be due to the different mechanisms that lead to the production of each emission product. But literature on this topic is sparse, and there are no sources to compare the profiles to than the ones mentioned in this work (Bekki et al. 2021; Larson et al. 2017). Since Larson et al. (2017) evaluated the NO$_x$ profile of a reentering rocket and Bekki et al. (2021) a reentering satellite the difference in ablation profile might also be due to the different reentry behaviours of these spacecraft. These profiles were then applied to the reentry trajectories. The first release point was set to 90 km since oxidation only happens starting from this altitude.

The emission profiles and trajectories were matched by altitude. Since the emission profiles and the trajectories do not have the same vertical resolution, the emission profile points were interpolated along the trajectory. To determine the amount of released mass fraction at each release point, the accumulated mass fraction within the interval from the previous point to the next point is calculated. All emissions that occur above 90 km were accumulated at the 90 km mark. For alumina emissions, this corresponds to 0.3 % and for NO$_x$ 0.1 % of the total mass emitted. This leads to slightly higher emissions at the 90 km mark than what would be seen in reality, but due to the fact that the atmosphere in the layer above 90 km is very thin, particles released at higher altitudes might descend quickly enough to make this a reasonable physical simplification.

Each object was then assigned the mass it was initialized with in GMAT. To get the absolute emissions, the mass loss fraction at each release point was scaled with the total mass of the object at each release point. It is commonly assumed in the literature that the emitted amount

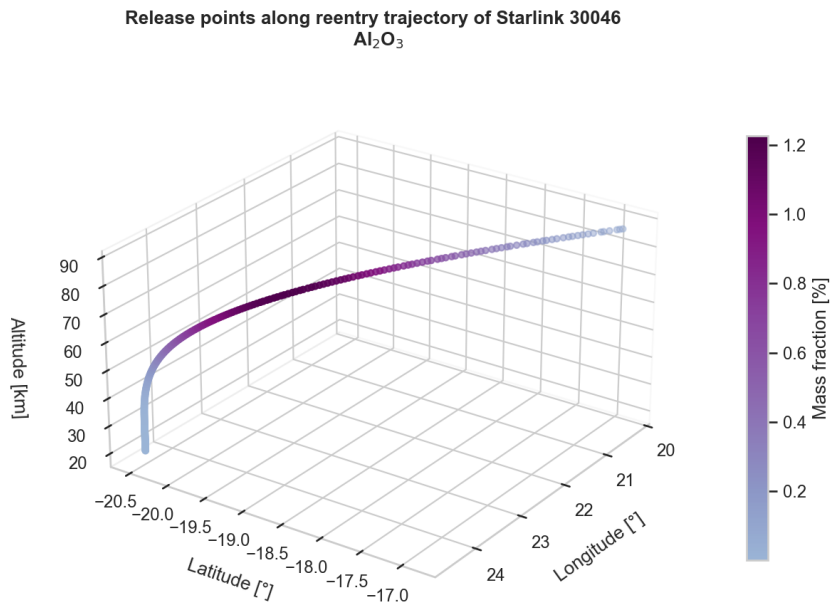

Figure 2.5.: Example of the injected alumina mass as a fraction of satellite mass as a function of latitude, longitude and altitude, for the example of Starlink satellite 30046. Emissions are discretized to 397 release points, at which mass is injected into the atmosphere, for the purpose of atmospheric transport modelling.

of NO_x is proportional to the total mass of reentering objects (Barker et al. 2024; Ryan et al. 2022). This then gives the final mass injected per release point as displayed in Figure A.2. Until this point, only the aluminum ablation was considered. Since alumina is a secondary product of the demise process, originating from the oxidation of the aluminium aerosols, it needs to be derived from the aluminium quantity.

First, the amount of mass that is injected into the environment is calculated following Equation 2.3. M is the total mass of the object, m_{Al}, set to 30 %, is the assumed mass fraction of aluminum in satellites, and d_{Al} is the demisability of aluminium parts, assumed to be 90 %.

$$M_{Al} = M\, m_{Al}\, d_{Al} \tag{2.3}$$

This then gives the injected amount of aluminum. Instant oxidation to alumina is represented in Equation 2.4 by the factor $C^{Al,AlO}$, which can take values between 0 and 1 for a

conversion rate of 0 % to 100 % from aluminum to aluminum oxide. M_{AlO} is the mass fraction of aluminum that is converted into aluminum oxide particles.

$$M_{AlO} = M_{Al}\, C_{Al,AlO} \tag{2.4}$$

In this work, further oxidation to alumina Al_2O_3 is then assumed. To then get the amount of $M_{Al_2O_3}$ mass that is emitted at each release point, the mass of the oxygen atoms M_O needs to be taken into account. Two aluminium molecules react to one alumina molecule. This means that the number of alumina $N_{Al_2O_3}$ molecules is equivalent to half of the number of present aluminium molecules N_{Al}. To get the emitted mass of alumina Al_2O_3, the mass of aluminium ablated needs to be scaled by the ratio of the molar weight of alumina $M_{Al_2O_3} = 101.96 \frac{g}{mol}$ to aluminium $M_{Al_2} = 53.96 \frac{g}{mol}$ i.e., a factor of 1.89. Since the trajectory and the emission profile do not have the same resolution, the theoretical total emitted mass deviates slightly from the actually emitted mass after interpolation. The total sum of released mass over all mass categories for NO_x is in theory 451,695 kg, but actually released in the model is 440,274 kg. This corresponds to a difference of 2.5 %. The alumina mass shows a 1.03 % deviation: in theory, it should be 73,737 kg, but actually released are 75,803 kg.
With the here derived emission profiles, global emissions could then be modelled by applying them to each satellite reentry trajectory. The zonal mean distribution of the emissions of all here modelled satellites can be seen for alumina and NO_x in Figure 2.6.

Since modelling the transport of these emissions accurately is computationally expensive, the atmospheric transport will only be modelled for one year of emissions (2015). However, the atmospheric transport will be simulated over six years (2015-2021), since this is approximately the time it takes for the emissions to be removed from the atmosphere. To evaluate the impact of continuous emissions over a 6-year period, monthly mean values for the years 2015-2021 are cumulated. For instance, concentrations for a month in 2021 will be calculated as the simulated concentrations in that month plus the concentrations in the same month for the years 2015-2020 – however, using emissions only in 2015. This effectively means that emissions are held constant over the years 2015-2021, and that the simulated concentrations are not valid for one specific year in this period but are rather representative for the whole period. Since a statistical approach was pursued to create the emission inventory, this should be a reasonable procedure to evaluate the overall transport processes in the atmosphere. However, interannual variations in transport cannot be evaluated.

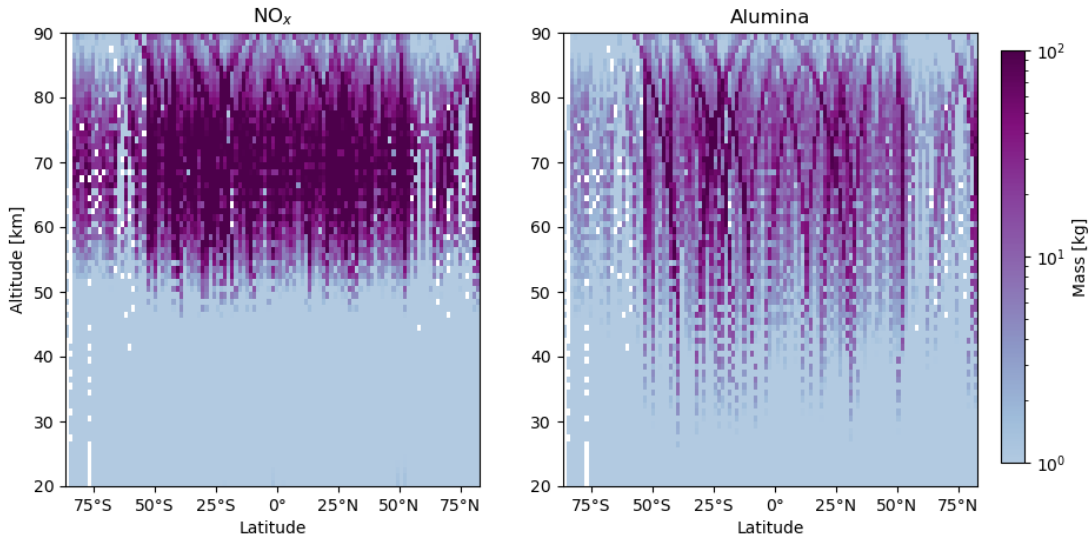

Figure 2.6.: Zonal mean of the alumina and NO$_x$ emissions in the first model year, with a grid resolution of 1° meridional and 1 km vertical.

2.4. FLEXPART

Airborne particles and gases that are emitted into the atmosphere will not remain at their source, but undergo a broad set of transport, deposition, and chemical processes. Atmospheric transport models are used to capture these effects. There are two types of atmospheric transport models: Either a Eulerian or a Lagrangian approach can be used. Using the Eulerian approach involves working with fixed grid points and evaluating the chemistry and airflow as net fluxes and changes. In contrast, the Lagrangian approach follows a particle and its trajectory through time and space. In this context, a particle is not a physical particle, but a computational particle representing an infinitesimally small air parcel. A caveat of Lagrangian models is that they rely on meteorological input fields, which can lead to propagation of errors from those fields (Bakels et al. 2024) and can only represent linear chemical reactions (Bakels et al. 2024). Eulerian models can represent a broader set of chemical processes, but are prone to numerical diffusion, which mitigates their ability to model long-range transport (Eastham et al. 2016). Lagrangian models can track individual plumes (Katharopoulos 2026) and have shown their superiority when it comes to modelling long-range plume dispersion (Bakels et al. 2024). As this study aims to investigate the distribution and transport of aerosols produced during spacecraft burn-up, using a Lagrangian model will provide the needed accuracy to model sharp gradients and filamentous structures which are expected to be seen. The FLEXible PARTicle dispersion model (FLEXPART) is a Lagrangian dispersion model that is often used to model the trajectory of air masses. Lagrangian particle dispersion models can resolve subgrid-scale processes by employing a parameterisation scheme.

The atmospheric transport of aerosols and gases is governed by two main processes: Advection, which describes the effect of the bulk motion from the surrounding air on a particle, and diffusion, which describes the stochastic motion due to turbulence. This can be formulated as the advection-diffusion equation (Eq. 2.5)(Tatsii 2025,Jacob 1999).

$$\frac{\partial \psi}{\partial t} = \underbrace{\nabla\left(D\nabla\psi\right)}_{\text{diffusion}} - \underbrace{\nabla\left(\mathbf{v}\psi\right)}_{\text{advection}} + R + C \tag{2.5}$$

In Lagrangian particle dispersion models, Eq. 2.5 is expressed from a Lagrangian perspective, where changes of the quantity ψ, can be expressed through all emission or deposition R and chemical processes C. This is described by the Lagrangian continuity equation (Eq. 2.6). Local temporal changes and advection of the wind vector v, are captured in the material derivative $\frac{D}{Dt} = \frac{\partial}{\partial t} + \vec{v}\nabla$.

$$\frac{D\psi}{Dt} = R + C \tag{2.6}$$

In FLEXPART, the frame of reference follows a particle's trajectory. These trajectories are described by Eq. 2.7, where the quantity ψ is the particle's position X.

$$\frac{dX}{dt} = v[X(t)], \tag{2.7}$$

Eq. 2.7 is integrated by assuming the "zero acceleration" scheme following Eq 2.8 by Stohl et al. (2005). This first order approximation of the particle's position vector after a time increment, Δt can be written as:

$$X(t + \Delta t) = X(t) + v(X, t)\Delta t \tag{2.8}$$

The wind vector v is composed of the grid scale wind, $\bar{v}$, the turbulent wind fluctuations v_t, and the mesoscale wind fluctuations v_m.
For particles with a non-zero mass, gravitational settling needs to be considered. This will change the particle's velocity, depending on the density ρ_p, diameter d_p and gravitational acceleration g. The gravitational force is counteracted by the drag force, following from the resistance the particle surface provides to the fluid. The impact that follows from these two forces is described by the terminal velocity, representing the particle's theoretical velocity when drag and gravitational force are in equilibrium. The size regime is important in this regard because the size of a particle influences how much turbulence is introduced to the fluid by the particle. The ratio of inertial to viscous forces in a flow is captured by the Reynolds number. For Reynolds numbers bigger than one, the terminal velocity is given by Eq. 2.9.

$$v_t = \sqrt{\frac{4\rho_p g d_p C_c}{3C_d \rho_f}} \tag{2.9}$$

For particles with Reynolds numbers smaller than one, this is given by Eq. 2.10.

$$v_t = \frac{\rho_p g d_p^2 C_c}{18\mu} \tag{2.10}$$

The Cunningham slip correction factor C_d accounts for non-continuum effects, and the empirically derived drag coefficient C_d is used in regimes with $Re \geq 1$, since the assumption of Stokes's law that inertial forces are negligible does not hold here. (Seinfeld et al. 2016), μ is the dynamic viscosity and ρ_f the density of the fluid.
To account for atmospheric removal, decay processes and deposition are also represented in FLEXPART. However, radioactive or chemical decay processes are neglected for the use case of this thesis. Deposition is the removal of a species from the atmosphere onto a surface. This can be due to wet or dry deposition. The removal of a particle by scavenging through precipitation is called wet deposition. This can refer to either ice and liquid water precipitation, and can occur in-cloud or below-cloud. Below-cloud scavenging is due to collision and coalescence with falling hydrometeors. In-cloud scavenging can be due to collisions, but also to aqueous-phase chemistry or nucleation and activation scavenging. The latter refers to the ability of aerosols to act as cloud condensation nuclei (CCN), which induce condensation of water vapour onto their surfaces and lead to the consecutive growth of water droplets. Due to the increase in mass, the droplet will experience gravitational acceleration, and will deposit from the atmosphere onto the ground; a similar effect is seen for ice crystals. The mass loss of a particle due to these different processes is represented, in Eq. 2.11, by an exponential loss depending on the scavenging coefficient Λ of each process (Pisso et al. 2019).

$$m(t + \Delta t) = m(t)exp(-\Lambda \Delta t) \tag{2.11}$$

Dry deposition, on the other hand, are all processes that are not due to interaction with hydrometeors, like gravitational settling, impaction, interception, and Brownian diffusion. (Seinfeld et al. 2016). Mass is lost by settling onto the Earth's surface. This is calculated by an exponential loss as well, which depends on the ratio of the deposition velocity and a reference height.
To drive FLEXPART, ERA5 data from European Centre for Medium-Range Weather Forecasts (ECMWF) with an hourly resolution and a $0.5° \times 0.5°$ grid is used as meteorological input (Hersbach et al. 2020). In FLEXPART, calculations can be done on terrain-following based vertical z-levels or on the ECMWF's hybrid pressure based η-levels. To avoid errors due to coordinate transformation and save computational resources, most processes, except for those in the atmospheric boundary layer, are calculated on η-levels (Bakels et al. 2024). ERA5 vertical levels are available from the surface to 1 hPa in pressure coordinates and 80 km for model level variables (Hersbach et al. 2020). ERA5 is a reanalysis dataset combining numerical weather prediction output with data assimilation of observational data. Using this as input into FLEXPART ensures that the Eulerian input fields have a high accuracy, and there are no data gaps. However, when considering processes that occur in the upper atmosphere, it is limited. One important source of assimilated data are radio soundings, which only reach the lower stratosphere. In higher layers, satellite radiance measurements are used. But these have the caveat that their weighting functions, accounting for the contribution of the atmospheric layer to the measured signal, decrease above the stratosphere. The mesosphere is considered observation-free and therefore prone to discontinuities, since there are no observations controlling the consistency between different ERA5 model runs. Known caveats of ERA5 in higher atmospheric layers are a cold bias in the lower stratosphere and a warm bias near the stratopause relative to assimilated observations, as well as an overly strong tropical westerly jet

in the mesosphere (Hersbach et al. 2020). The vertical resolution of the reanalysis decreases with altitude, which further limits the reliability of the meteorological fields. This will have an impact on the representation of transport processes in this region.

2.4.1. FLEXPART set up

As discussed in the preceding section, FLEXPART relies on reanalysis data, which is only available for the past. To be able to model a horizon of 6 years, the beginning of the simulation needs to be shifted into the past. Therefore, satellite reentry emissions will be released in 2015. This will not represent the actual emissions of 2015, but a representative distribution of the average reentry activities over the period 2021-2025. The total modelled time period will be from 1 January 2015 to 1 January 2021, one year of emissions followed by five years, to allow enough time for the emissions to be (almost completely) removed from the atmosphere.
In a last step, the FLEXPART release files need to be created. For this, each species that is released needs its own species file. These define the aerodynamic properties of the species. The release file, part_ic.nc, defines the coordinates, number of computational particles, and time of each release point. About 30 Mio. particles are released in total per species. Each species is then run in an individual simulation. For the part_ic.nc file, the number of released particles needs to be defined at each release point. This is done by dividing the total emitted mass by the number of computational particles used to obtain the mass of a single computational particle, from which the number of particles equivalent to the emitted mass at that point is derived. Three species for alumina emissions are defined. An alumina air-tracer species to represents particles with a diameter smaller than 1 nm accounting for the particles that are emitted by alumina evaporation due to high surface temperatures. At this size, gravitational settling can be neglected. This is supported by the settling velocities shown in Figure A.7. At 80 km altitude, particles with a diameter of 0.1 nm have a settling velocity of approximately 10^{-4} m/s, which corresponds to about 10 m/day. To account for the aerosols that are produced by secondary oxidation and coagulation in the reentry plume two species with larger diameter are defined: One with a diameter of 50 nm, and one with a diameter of 100 nm (Murphy et al. 2023). The density is set to that of alumina: 3.95 $\frac{g}{cm^3}$ (Matori et al. 2012). The geometry of the aerosols is assumed to be spherical. The remaining parameters were taken from the "Aerosol" species file and can be found in Table 2.2. To represent NO_x the already existing nitrogen dioxide species is used.

The most important parameters for Al_2O_3 aerosols are described in the following paragraph. Since wet and dry deposition processes are parametrized in FLEXPART, the scavenging efficiencies for each of these need to be defined. For wet deposition of aerosols, PCRAIN and PCSNOW represent the below-cloud scavenging, rain and snow collection efficiencies, accounting for the removal through precipitation. Similar to that, the alumina tracer for below-cloud scavenging processes PWETA_GAS sets the gas wet deposition for a precipitation of 1 mm h^{-1}, and PWETB_GAS depends on the precipitation rate. PCCN and PIN, on the other hand, represent in-cloud scavenging by parameterizing the cloud condensation nuclei efficiency and ice nuclei efficiency. The geometric standard deviation of the particle diameter is set by PDSIGMA, influencing the deposition velocity, and therefore governing the dry deposition process. The

dry deposition, is defined as the ratio between the diffusivity of H_2O and the species, is set by PRELDIFF. For gas dry deposition and in-cloud scavenging, the Henry constant is employed to describe how soluble a gas is in a liquid, the reactivity for oxidation; for biological substances relative to that of ozone is set to zero.
The output grid resolution is $1^\circ \times 1^\circ$ with a vertical resolution of 1 km. The model domain covers the whole globe.

Parameter	**Value**	**Unit**
Al_2O_3		
PCRAIN_AERO	1.0	1
PCSNOW_AERO	1.0	1
PCCN_AERO	0.9	1
PIN_AERO	0.1	1
PDSIGMA	1.25	1
$Tracer$		
PWETA_GAS	$6.28 \cdot 10^{-5}$	$1 s^{-1}$
PWETB_GAS	0.62	1
PRELDIFF	1.9	1
PHENRY	1.3	$M\ atm^{-1}$
WEIGHTMOLAR	101.0	$g\ mol^{-1}$
PF0	0	1
NO_x		
PWETA_GAS	$7.12 \cdot 10^{-5}$	$1 s^{-1}$
PWETB_GAS	0.62	1
PRELDIFF	1.6	1
PHENRY	$1.0 \cdot 10^{-2}$	$M\ atm^{-1}$
PWEIGHTMOLAR	46.0	$g\ mol^{-1}$
PF0	0.1	1

Table 2.2.: Parameter values for the respective species files

3. Results and Discussion

The goal of this work is to explore how emissions from satellite reentries are distributed in the atmosphere, by employing the Lagrangian transport model FLEXPART. For this purpose, global reentries over the course of one year were considered, and their transport simulated for 5 more years. Alumina particles and nitrogen oxides hold the largest share of emitted substances, and are therefore analysed. To evaluate the effect of particle size on atmospheric lifetime and deposition regions three different alumina species were defined: 1) an alumina tracer, which can be assumed to have no gravitational settling; 2) Particles in the Aitken mode, with 50 nm diameter; and 3) particles at the onset of the accumulation mode, with 100 nm diameter. This section will discuss the results from these simulations and is structured as follows: First, the overall global transport patterns and their seasonality are discussed by comparing the state of the atmosphere in July with January of each year. Here, the zonal mean of the mass mixing ratio and the mass concentration are considered. Following this, deposition patterns are discussed in Section 3.2.1. This section will focus on the difference between wet and dry deposition, as well as the impact of reentry location on the location of deposition. Next, the sensitivity of transport and deposition patterns on the particle size will be discussed in section 3.2.2. NO_x is regarded in a separate section (Section 3.3).

3.1. Alumina

3.2. Transport and seasonality

This section focuses on the 50 nm species to explore transport patterns, which are similar between all three alumina species. In a later section, emphasis will be placed on the differences that arise from varying particle sizes. A total of 75 t of alumina was released between 90 and 20 km. The bulk of emissions is released in the main ablation region of reentering spacecraft, between 80 and 40 km. To represent the state of the atmosphere after 6 years of continuous emissions, Figure 3.1 shows the respective six-year sums of January and July values. The main accumulation region is in the mesosphere, close to the origin of the emissions, and extends into the polar stratosphere of the winter hemisphere. Towards lower altitudes, the mass mixing ratio is decreasing. Comparing the distribution in January to July, the transport of air masses towards the winter pole is visible. January shows stronger downward transport and a more vertically widespread region of higher mass mixing ratios, in comparison to July. Maximum values reach 154 pg/g at 61 km and 80°S in July, and 116 pg/g at 48 km and 85°N in January. In January, the height of the upper boundary of particle concentration shows a descent from South to North Pole. Whilst particles can be found up to nearly 80 km on the South Pole, the vertical distribution only extends to 60 km on the North Pole. The opposite

behaviour is found in July. This pattern is due to the BDC transporting air masses towards the South Pole in the SH-winter, and descent into lower atmospheric layers there. The January plot shows the NH-winter, when the northward transport in the deep-branch of the BDC is getting stronger and transports more mass towards the North Pole. Similar structures are found for the mass concentration. The mass concentration shows the highest values in the stratosphere. Maximum values at the NH winter pole are higher, and are observed at higher altitudes: 152 pg/m^3 at 47 km and 85°N, than at the SH winter pole: 95 pg/m^3 in July at 28 km and 77°S.

The tropics show lower mmr compared to the mid and high latitudes. This has two causes: on the one hand, the Tropics are largely free of satellite debris; on the other hand, atmospheric circulation patterns lead to transport out of the Tropics. At lower altitudes, this is due to the higher tropopause, which extends up to 18 km in the Tropics, and the fact that particles are quickly scavenged in the troposphere. Above the tropopause, the BDC transports air masses originating from the troposphere upward in the tropics and towards the mid and high latitudes in the strato- and mesosphere. During transport, filamentous structures and sharp concentration gradients develop within the emission fields. This behaviour is illustrated in Figure 3.2, which shows the spatial distribution of the mass mixing ratio after the first year of emissions at different altitudes. In particular, at 25 km and 30 km altitude, streaks of enhanced concentrations can be observed adjacent to regions with lower concentrations, indicating the presence of pronounced gradients.

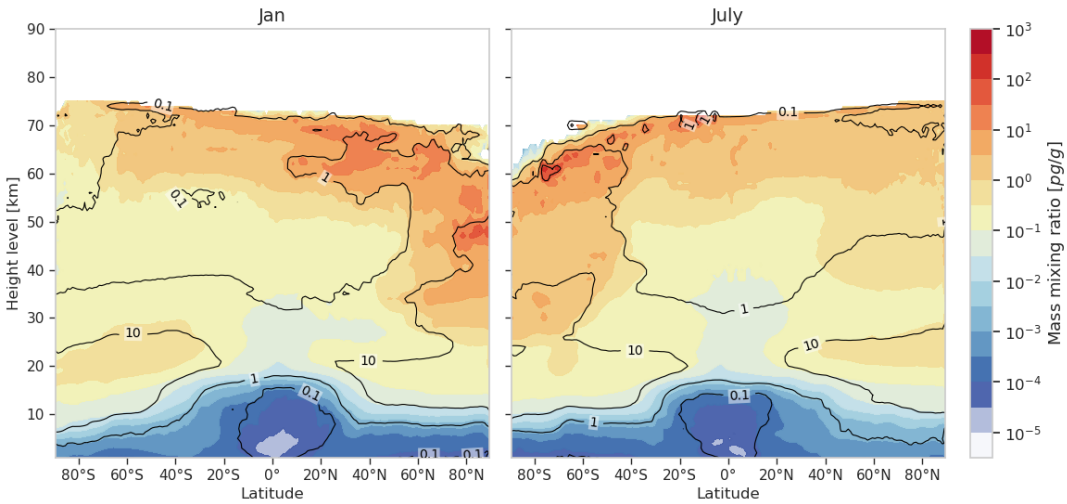

Figure 3.1.: Zonal mean mass mixing ratio of alumina particles with a diameter of 50 nm. The left panel shows the six-year sum of January values, and the right panel shows the six-year sum of July values. Mass concentration is shown by the black contour lines in pg/m^3.

The evolution of emissions throughout their atmospheric lifetime can be seen in Figure 3.3. In this figure only one year of emissions is considered and then evaluated over the modelled

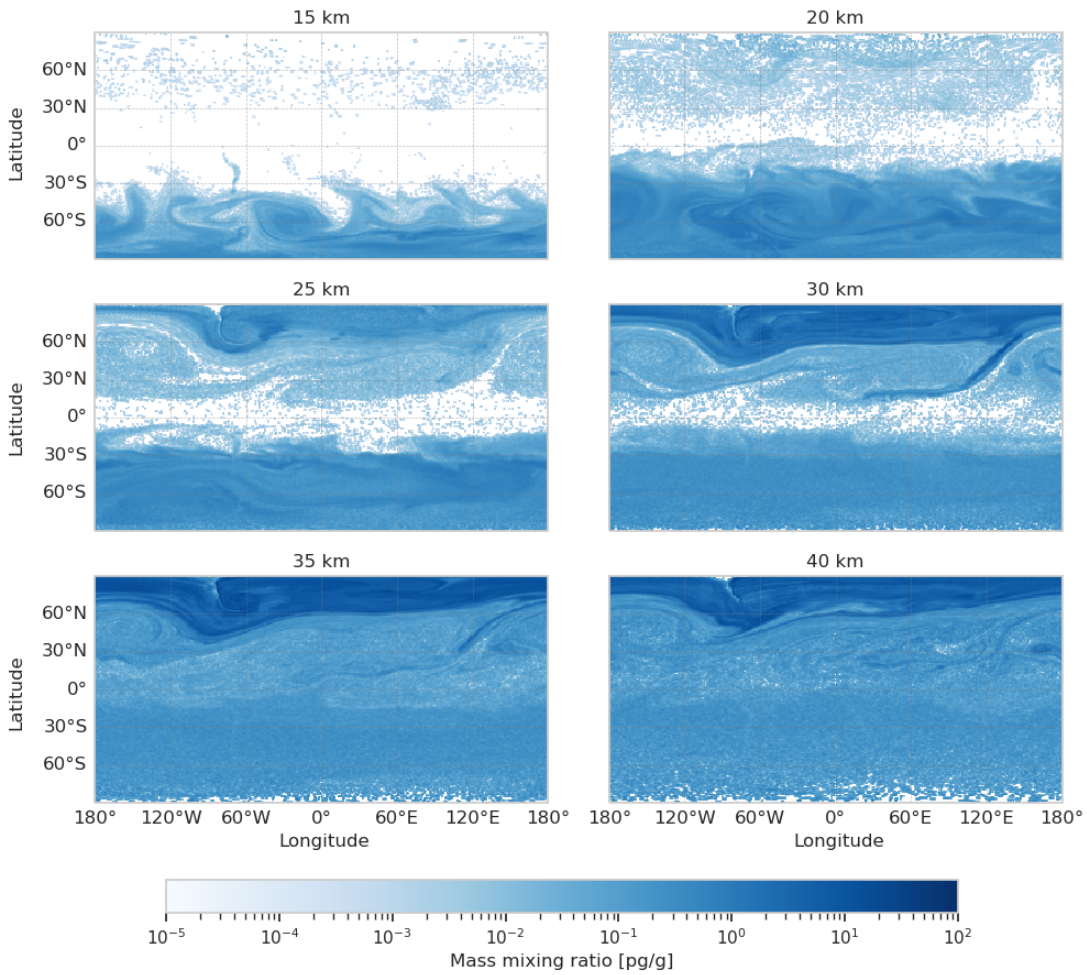

Figure 3.2.: Mass mixing ratio of alumina particles with a diameter of 50 nm, at different altitudes, at the end of the first year of emissions.

period. These plots illustrate the atmospheric states at the time indicated at the top of each subplot. Each panel represents the 15 December of that year. The vertical profile of the zonal-mean mass concentration is displayed for particles with a diameter of 50 nm. In the first year, 2015, the emissions are well distributed through all atmospheric layers, with regions of high concentrations and mass mixing ratios at the poles and at the highest model layers. Later, ongoing deposition reduces the atmospheric burden over time.

At the end of the second year, 2016, the bulk of particles has shifted towards lower altitudes. The tropics still show a lower mmr than the mid latitudes, the poles higher mmr, with higher values in the North Pole winter maximum than the South Pole. In the mesosphere, the tilt towards the winter hemisphere pole is still visible. In later years, the North Pole shows lower values in the stratosphere than the South Pole, showing enhanced downward transport. The

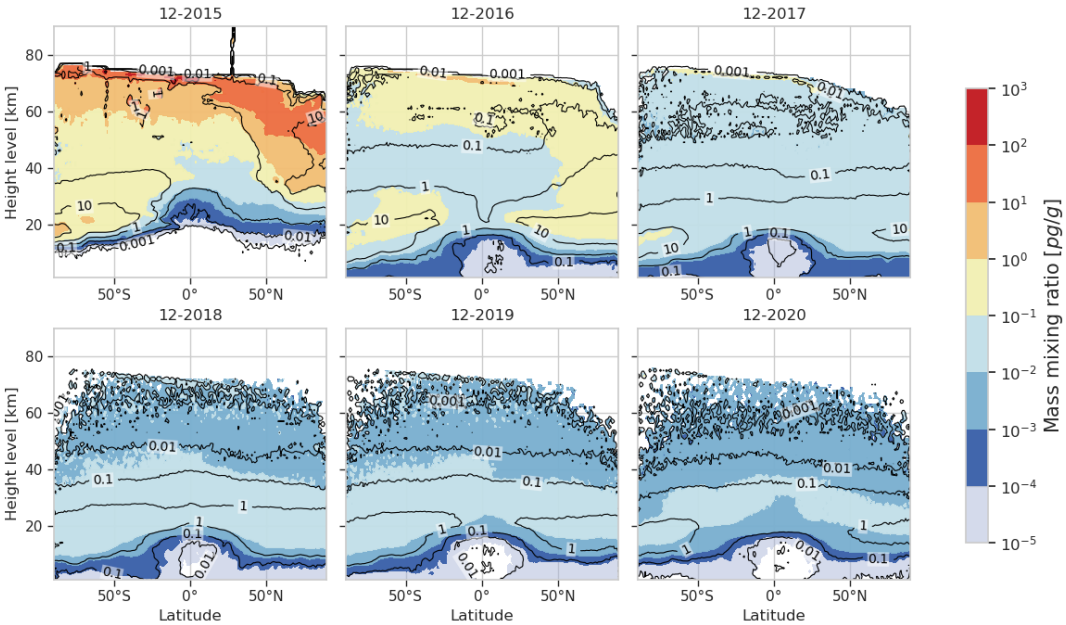

Figure 3.3.: Mass mixing ratio of the vertical distribution of the zonal mean of the alumina particles with a diameter of 50 nm in December for the time period of 2015-2020. Mass concentration is displayed by the black contour lines

continuous decrease of mixing ratio values through the years points towards deposition of particles out of the atmosphere onto the surface.

The descent of the particles through the atmosphere is well represented by comparing the altitude of the lower boundary of the plume in December 2015 to the next year which changes from 20 km to surface level. Below 10 km, the distribution is sparse, with concentrations lower than 10^{-3} pg/m^3, showcasing that most of the released mass resides above the tropopause. Particles entering the troposphere are rapidly removed from the atmosphere via efficient deposition processes. This behaviour is evident in Figure 3.4, which shows global mean vertical mass concentration profiles based on accumulated emission over the 6-year model period. The profiles indicate that particles undergo rapid downward transport through the mesosphere, with peak mass concentrations in the stratosphere. From this region, particles are subsequently scavenged within the troposphere.

The effect of reentry location on the atmospheric transport can be seen in Figure A.5 and Figure 3.5. Both plots show, similar to Figure 3.1, the accumulated values of every January or July, respectively. Differences in the mass mixing ratio are evident between the different reentry locations, while the effect of the global circulation remains visible. Mass accumulates at the winter pole, but enhanced concentrations are still present in the reentry regions. In Figure 3.5, the panel showing polar SH reentries in July is an exception, since higher values at North Pole are prominent. This is likely due to most SH polar reentries occurring in the second half of the year, which can also be seen by the comparable high values in this region in January

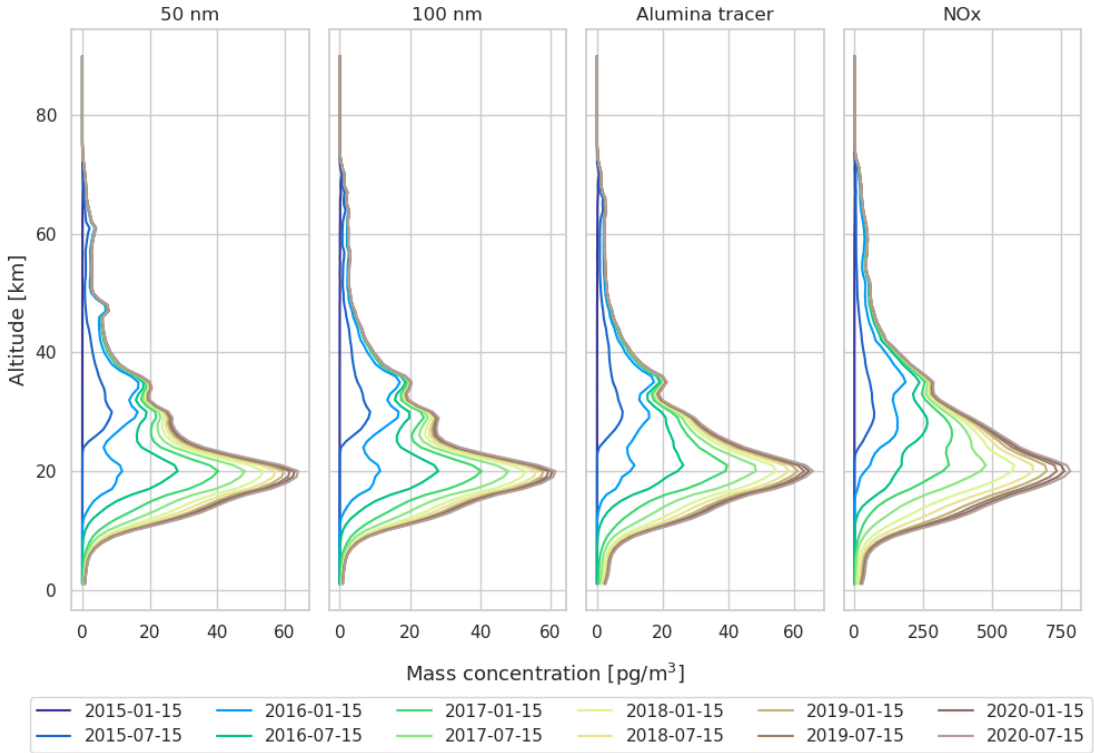

Figure 3.4.: Global average vertical mass concentration profiles, accumulated for the indicated timestamp and the corresponding dates from previous years.

(Figure A.5). In the other regions, reentries are more well distributed throughout the year. In this case, January emissions at the South Pole are transported towards the North Pole, while no new emissions are added to be then transported towards the South Pole in the SH winter. The distribution for January complements this well: high and very concise emissions from satellites are present in the mass mixing ratio with pronounced transport towards the North Pole. It is evident that even polar reentries are distributed over the whole globe. This shows that the transport patterns of the space debris emissions are highly dependent on atmospheric circulation as well as the reentry location and season.

The theoretically calculated settling velocities for alumina particles with different diameters are displayed in Figure A.7. The concentrations in the mesosphere are decreasing quicker than at lower altitudes due to the increase of settling velocity with increasing altitude. Transport is influenced by the rate of vertical motion of the air parcels particles are suspended in. These can either enhance the atmospheric lifetime by upward transport or decrease it through downward transport, carrying the particle downward. The ERA5 climatological mean of the vertical motion, for June, July and August, as well as for December, January and February, can be found in Figure A.6. These show the mean over the winter months at each pole. The BDC is clearly visible through downward transport at each winter pole. In the upper mesosphere,

the settling velocities of particles with a diameter of 100 nm and 50 nm are one magnitude higher, with about 100 mm/s, than the rate of vertical motion of the air parcels, with about 10 mm/s. The settling velocities decrease towards lower altitudes. At 60 km, they are at the same magnitude as the vertical velocity of the air particles. The particle motion will be therefore influenced by the motion of the air particles it is currently suspended in. This leads to atmospheric circulation patterns having a major impact on transport.

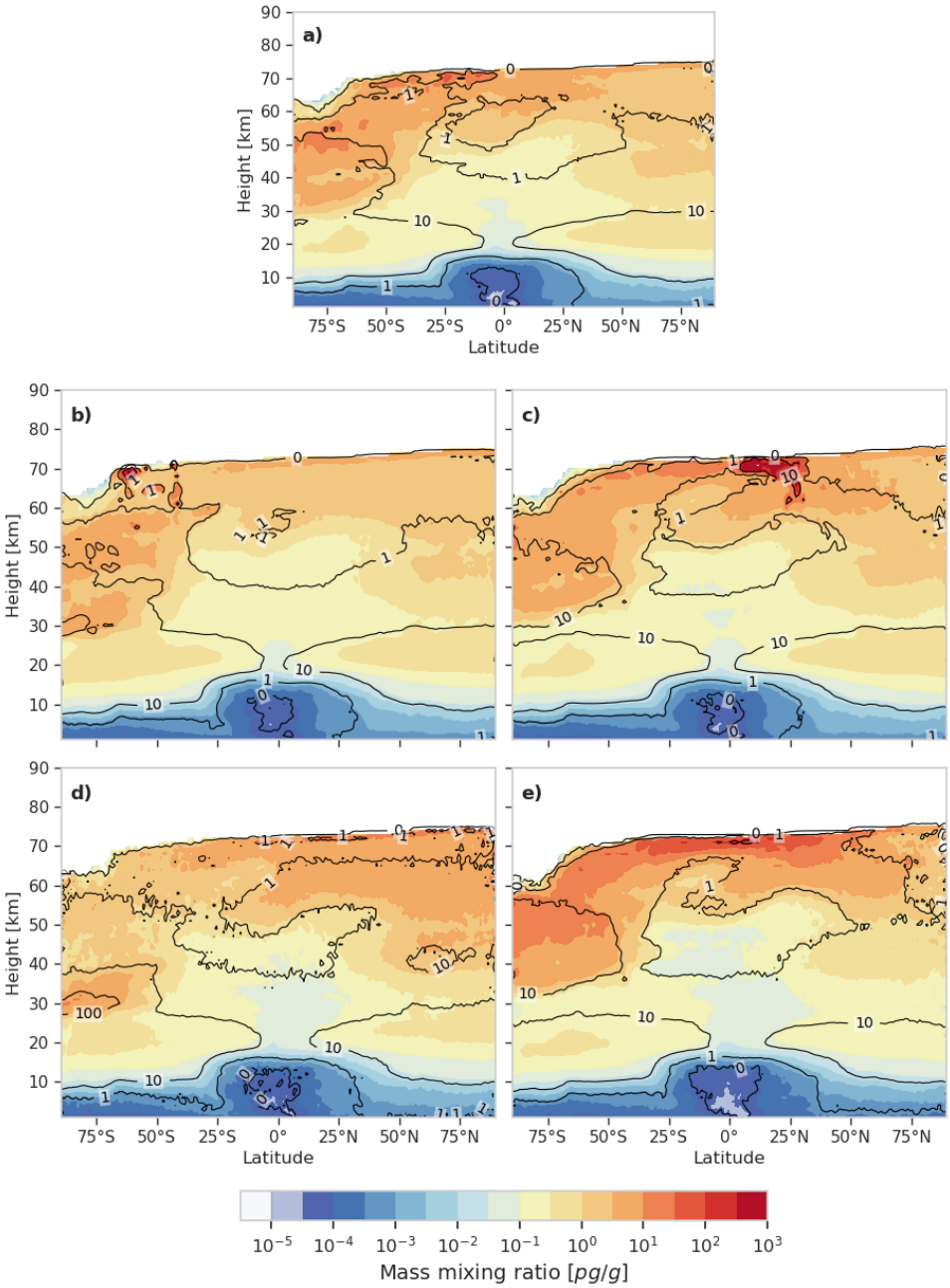

Figure 3.5.: Six-year sum of the zonal-mean mass mixing ratio of alumina particles with a diameter of 50 nm, for July. For each subplot, only reentries within the indicated region are considered: (a) tropics, (b) subtropics and mid-latitudes in the Southern Hemisphere, (c) subtropics and mid-latitudes in the Northern Hemisphere, (d) polar region of the Southern Hemisphere, and (e) polar region of the Northern Hemisphere. Each region is scaled by the fraction of total mass relative to the emitted mass in the respective region. Mass concentration is displayed by the black contour lines in pg/m^3.

3.2.1. Deposition

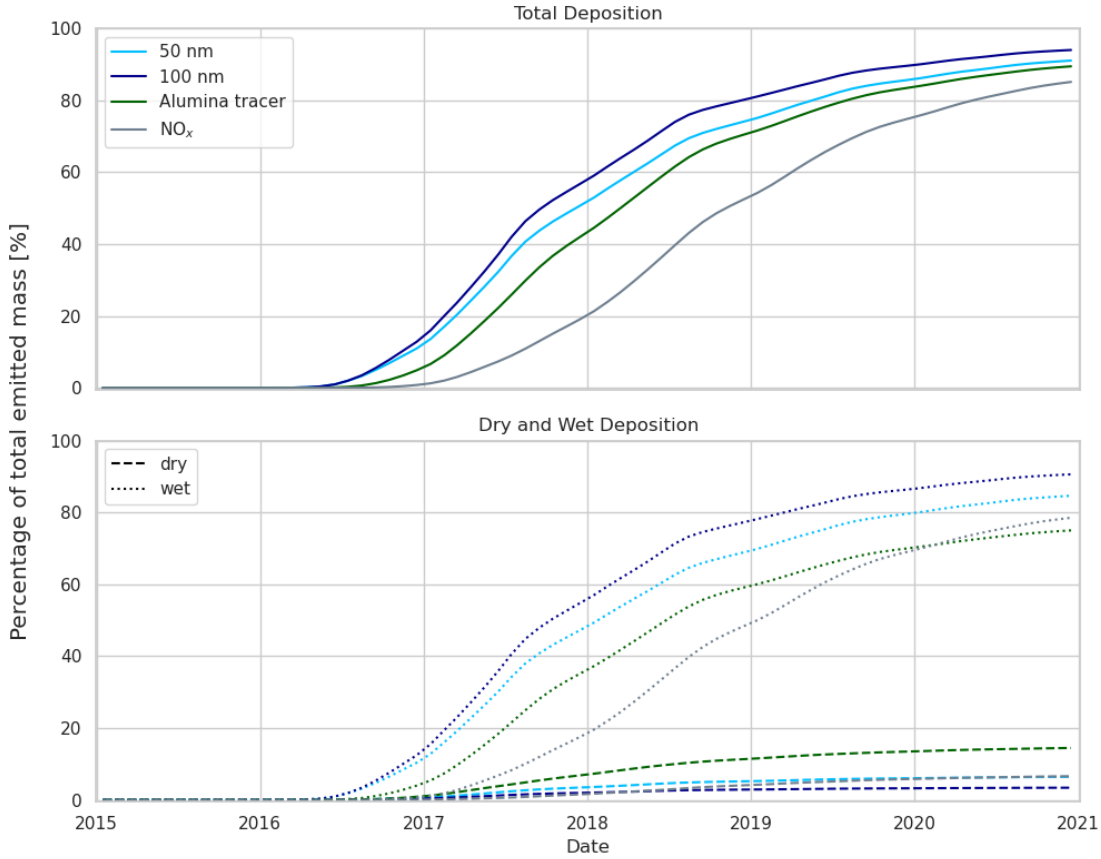

Figure 3.6.: Deposited mass as a function of time, shown in percentage of the total emitted mass. The total deposited mass is given as the sum of wet and dry deposition in the upper panel. The individual deposition modes are shown in the panel below.

Figure 3.6 shows the accumulated deposition per species as a function of the time passed since simulation start. In the first one and a half years, deposition is close to zero since few particles have reached the troposphere. From the middle of the second year onwards, alumina particles with diameters of 50 nm and 100 nm start to show a significant amount of deposited mass. Given that the first emissions occur at the beginning of 2015, it took about 1.5 years from the first emission to deposition. The first 20 % of mass are deposited after two years. 50 % of mass has been deposited after two and a half years, and 80 % after four years. The remaining 10 % are deposited within the last two years at equal rate. 10 % of mass are not deposited and remain in the atmosphere at the end of the simulation time. This makes the year 2017, with 40 % of all deposition, the year with highest deposition. Therefore, it can be concluded that the atmospheric lifetime of the alumina particles is about 1.5 to 2 years on average. The alumina tracer shows a different picture. First deposition signals can be seen only at the end of the year

2017, and start to increase slower than those of the alumina particles. This behaviour is closer to the settling characteristics of a gaseous species like NO_x than to the alumina particles. The alumina tracer still shows a different deposition pattern than NO_x, since they do not have the same emission regions (see Figure 2.6). The alumina tracer emissions reach lower altitudes than the NO_x emissions, which explains the earlier onset of deposition.
Particles with 100 nm show the highest deposition at the quickest rate, then the particles with 50 nm, and the lowest values can be seen for the Alumina tracer. The amount of deposited mass is continuously increasing over the next two years, and then plateaus. Final deposition values are displayed in Table 3.1. The amount of mass that is already settled, or still suspended in the air, for each species is shown for the last model time step. In general, most of the original emitted mass is already settled at the end of 2020.

Species	Airborne	Deposited	Airborne + Deposited	Emitted	Difference
100 nm	4 411	71 356	75 767	75 790	23 (0.03 %)
50 nm	5 556	69 156	74 712	75 790	1 088 (1.42 %)
Alumina tracer	6 092	67 943	74 035	75 790	1 755 (2.32 %)
NO_x	63 069	374 966	438 035	440 274	2 239 (0.51 %)

Table 3.1.: Total mass per species that is either still suspended in the atmosphere (airborne), or deposited, as well as the sum of both, and the difference of the sum to the original released mass. The deviation between the sum of airborne and deposited mass to the total released mass is given in percentages in the same column. The difference indicates mass missing to the total emitted mass. All values are given in kg and for the end of the simulation.

The combined amount of wet and dry deposition is illustrated in Figure 3.7 for particles with a diameter of 50 nm, in Figure A.8 for particles with a diameter of 100 nm and for alumina tracer particles in Figure A.9. The spatial distribution of the locations of high deposition values is comparable for all three alumina species. In both hemispheres, the bulk of mass is deposited in the mid-latitudes between 70°-30°. The high Antarctic, the equatorial Pacific, the Saharan Desert, as well as along the coastline of south-west Africa, show substantially lower amounts of settling. Along the equator, strong uplift happens due to the strong solar radiation, which induces heating and uplift; this induces strong convective behaviour of the air masses in general, inducing uplift of particles, transporting particles away from the equator, and inhibiting settling. These patterns are a result of the global circulation. Air descends in dry intrusions from the high-latitude stratosphere into the mid-latitude troposphere.

Particles are deposited there and never reach the Tropics, nor the Arctic or Antarctic. Dry intrusions occur only in the mid-latitude storm track, and therefore never reach the Saharan desert. Storm tracks are characterised by cyclones following a north-east trajectory in the Atlantic, leaving a region of sparse precipitation where they do not pass. The southern part of the Andes and the Antarctic Peninsula show especially high deposition values, since these regions

are at the downstream end of the storm tracks. Additionally, the mountainous topography plays an important role for the deposition. Other mountain regions show high deposition values as well, as seen in the Rocky Mountains in North America, the Alps in Europe, the Himalayas in Asia, and the Ethiopian highlands. This is due to the influence of mountain ranges on local weather patterns. Orographic lift leads to cooling and increased precipitation rates. The elevated topography also acts as a barrier for air masses, leading to an increased residence time, and therefore enhanced deposition. This pattern is present for all three alumina species.

For all species, more mass is deposited in the southern hemisphere. For particles with a diameter of 50 nm: 55 %, for a diameter of 100 nm: 53 %, and for the alumina tracer: 54 %, of the total deposited mass settles in the SH. This is to be expected, since about 58 % of the total emitted mass is released in the SH. About 18 % of all released mass is from satellites that reentered in the tropics, within a latitude range of 15°S to 15°N. 43 % of all emitted mass is distributed in the subtropical bands (20° to 35°) in both hemispheres. 31 % of the mass is from satellites that reentered in the mid-latitudes (35° - 60°). About 8 % is released within the polar circles, with latitudes larger than 60°. Whilst the most mass is deposited in the mid-latitudes, this is not the area where the most mass was released.

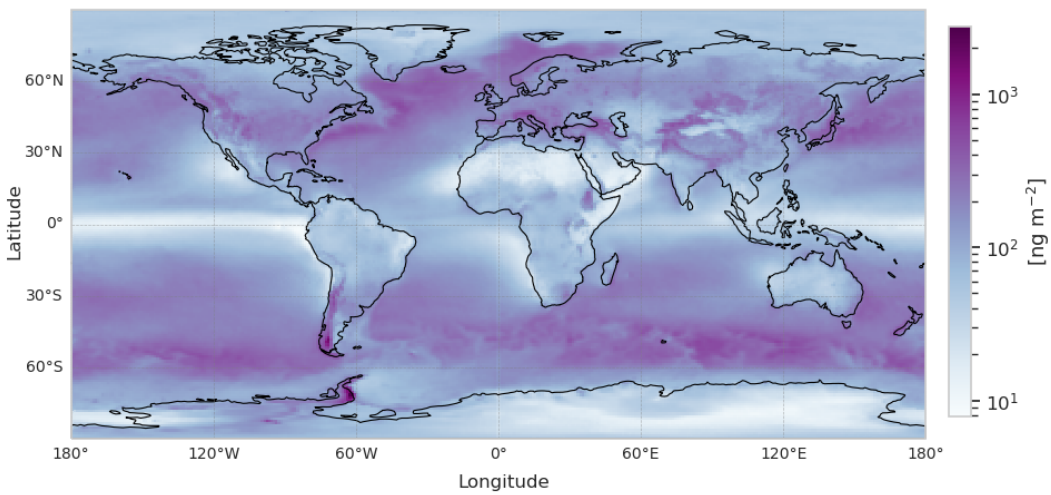

Figure 3.7.: Spatial distribution of deposited mass in ng/m^2 of particles with a diameter of 50 nm, at the end of the modelled period.

As discussed in section 2.4, there are two main deposition pathways for aerosols: wet deposition and dry deposition. In the following, the impact of these processes on the results will be evaluated. Figure 3.8 shows the percentage of wet deposition of the total deposition at the last time step. Therefore, regions with low values see higher dry deposition. The Saharan desert, as well as the Arabian Peninsula, South Asia and West Australia, see more dry than wet deposition, well in line with the lower than average precipitation values in these regions. Particles with a diameter of 100 nm show overall the same pattern, with a trend towards more dry deposition compared to the 50 nm particles (see Figure A.11).

Further regions with dominating dry deposition can be identified along the west coast of the African continent. That is well in line with the area that is not covered by the Atlantic storm tracks. The extended region of higher dry deposition from the Equator along the South American west coast can be well associated with cold upwelling water, inhibiting precipitation as well. The alumina tracer particles show especially high dry deposition values along coastal lines. When considering the deposition patterns, a clear difference can be made out between the aerosol species and the gas tracers. In Figure A.12, increased dry deposition amounts can be seen on the West Coast of North and South America, on the West Coast of North and South Africa, on all coastlines of the Arabian Peninsula, and on the West Australian coast.

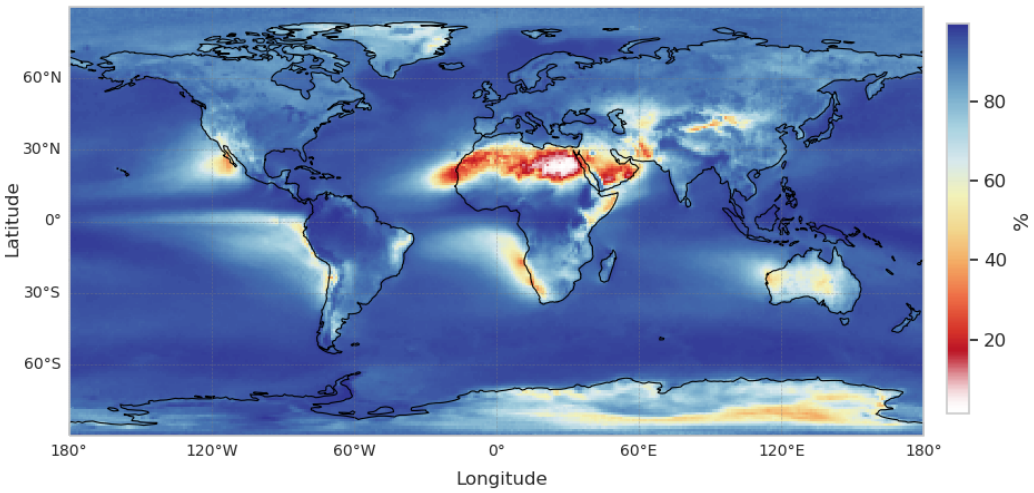

Figure 3.8.: Percentage of wet deposition of the total deposition. Accumulated after 6-years of emission of particles with a diameter of 50 nm.

3.2.2. Size sensitivity

The mean transport of particles with a diameter of 50 nm shows comparable transport patterns to those of 100 nm and the alumina tracer. Areas of high mixing ratios at the poles, the tilt towards the pole of the winter hemisphere, and the lower mixing ratios in the tropics can be identified. It can be noted that, in the lowest 20 km, the alumina tracer particles show higher mass mixing ratios than the species with higher diameter. This becomes evident when comparing, e.g., the area with mmr of 10^{-4} pg/g and 10^{-3} pg/g in Figure A.4 to Figure A.3. Further, the maxima in the zonal mean accumulated mass mixing ratio in December of 2020 after 6-years of continuous emissions can be compared: 100 nm: 382 pg/g, 50 nm: 358 pg/g, alumina tracer: 269 pg/g. These values are all seen at an altitude of 74 km. Due to quicker settling into regions where additional emissions occur, the particles with larger diameters show higher mmr. When comparing this to the emissions of one single year propagate over the simulated period: 100 nm: 4.9 fg/g, 50 nm: 6.4 fg/g, Alumina tracer: 102 fg/g, it becomes visible

that now the Alumina tracer particles show the highest mmr of the three alumina species. This is well in line with the lower settling velocities and longer atmospheric lifetimes that are expected for these particles. In addition to that, the comparison of the total deposited mass at the end of the simulation time for different species (Table 3.1) can be evaluated. The 100 nm species exhibits the highest deposited mass, at approximately 71 t, followed by the 50 nm species with around 69 t. The alumina tracer particles show the lowest deposited mass, at approximately 68 t. This indicates that particles with a bigger diameter have a shorter atmospheric lifetime than particles with a smaller diameter. In conclusion, particles with a smaller diameter show higher mass mixing ratios that are more persistent in the atmosphere, in comparison to particles with a bigger diameter, which show lower mass mixing ratios and shorter atmospheric lifetimes. Figure 3.6 shows that the alumina tracer particles exhibit the highest wet and the lowest dry deposition values among the three alumina species. This is also a result of their lower gravitational settling speeds. In contrast, particles with a diameter of 100 nm show the highest dry deposition, and the lowest wet deposition, demonstrating the opposite behaviour.

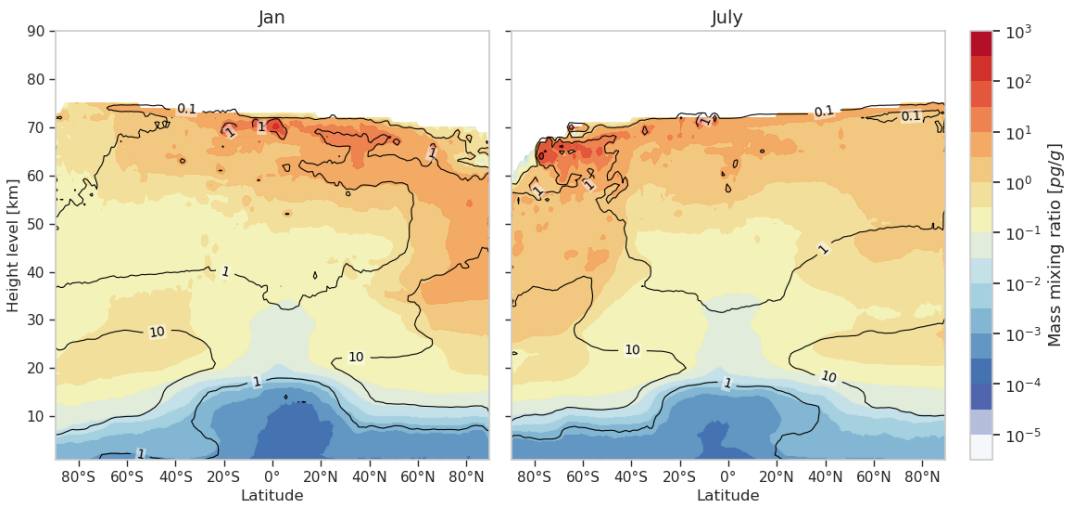

Figure 3.9.: Zonal mean mass mixing ratio of the alumina tracer. The left panel shows the six-year sum of January values and the right panel shows the six-year sum of July values. Mass concentration is shown by the black contour lines in pg/m^3.

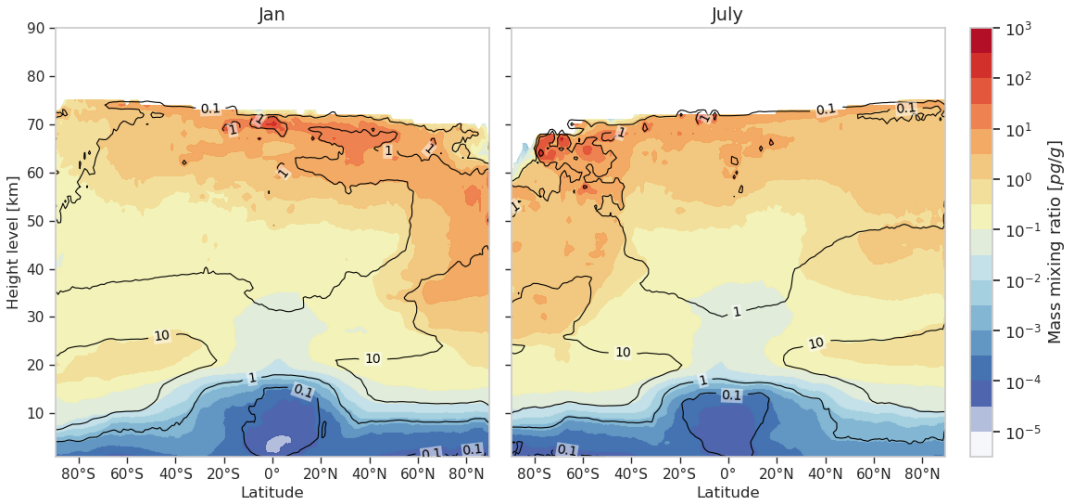

Figure 3.10.: Zonal mean mass mixing ratio of alumina particles with a diameter of 100 nm. The left panel shows the six-year sum of January values, and the right panel shows the six-year sum of July values. Mass concentration is shown by the black contour lines in pg/m^3.

3.3. NOx

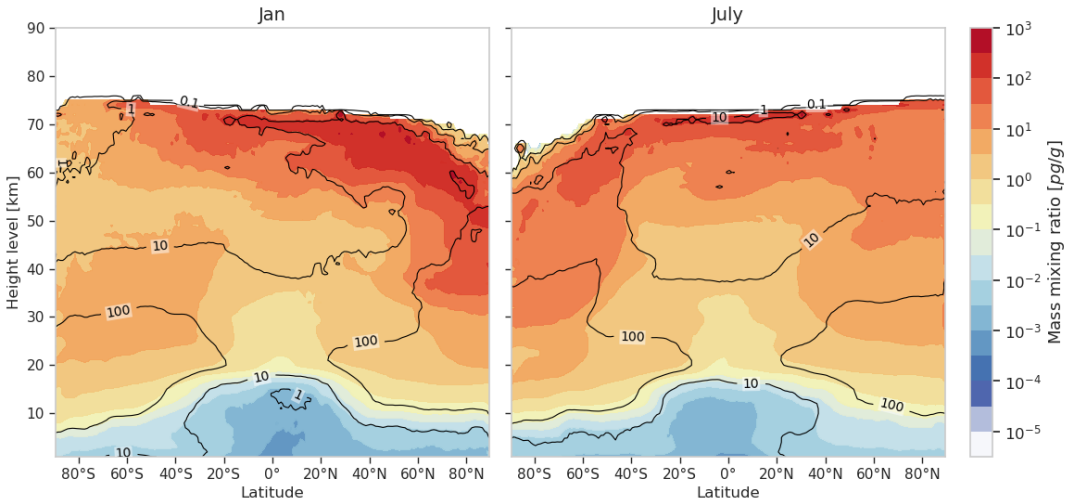

Figure 3.11.: Zonal mean mass mixing ratio of NO_x. The left panel shows the six-year sum of January values, and the right panel shows the six-year sum of July values. Mass concentration is shown by the black contour lines in pg/m^3.

NO_x, in comparison to the alumina aerosol species, is a gas and therefore exhibits different mechanisms governing its transport. This can be observed in Figure 3.4. NO_x shows a larger spread in its vertical mass concentration profile, pointing towards weaker vertical transport than the other species. It is evident that more mass is released than for the other species, as seen (in Figure 3.11) by the overall higher mass mixing ratios. The mass concentration shows values up to 10^3 pg/m^3, which is one magnitude higher than for the other species. Analogous to the other species, high values at the upper boundary of the plume are observed.
Figure 3.12 shows the evolution of one year of emissions over the whole modelled period. Most of the descent happens within the first three years, but mass mixing ratios up to 1 pg/g can still be seen in the upper mesosphere, as well as in the stratosphere towards the end of the simulation period. Further, the time series of deposited mass (Figure 3.6) illustrates that NO_x deposition occurs over longer timescales, as can be seen by the shifted onset of deposition values. About 40 % of all deposited mass settles in the fourth simulation year, one year later than the alumina species with larger particle diameters. In the following year about 30 %, and in the last year, 10 % of all deposited mass has been deposited. The total deposited mass at the end of the simulated time period is 374 t (Table 3.1). This is about 85 % of the original released mass. It suggests that the fraction of the mass that is still airborne has a longer atmospheric lifetime than the 5 simulated years. The main mode for deposition is wet deposition, with only about 10 % of all deposited mass being due to dry deposition processes.

Overall, NO_x shows the same global transport patterns as identified in the other species: the BDC transporting air masses pole ward and lower mixing ratios in the tropics. As already

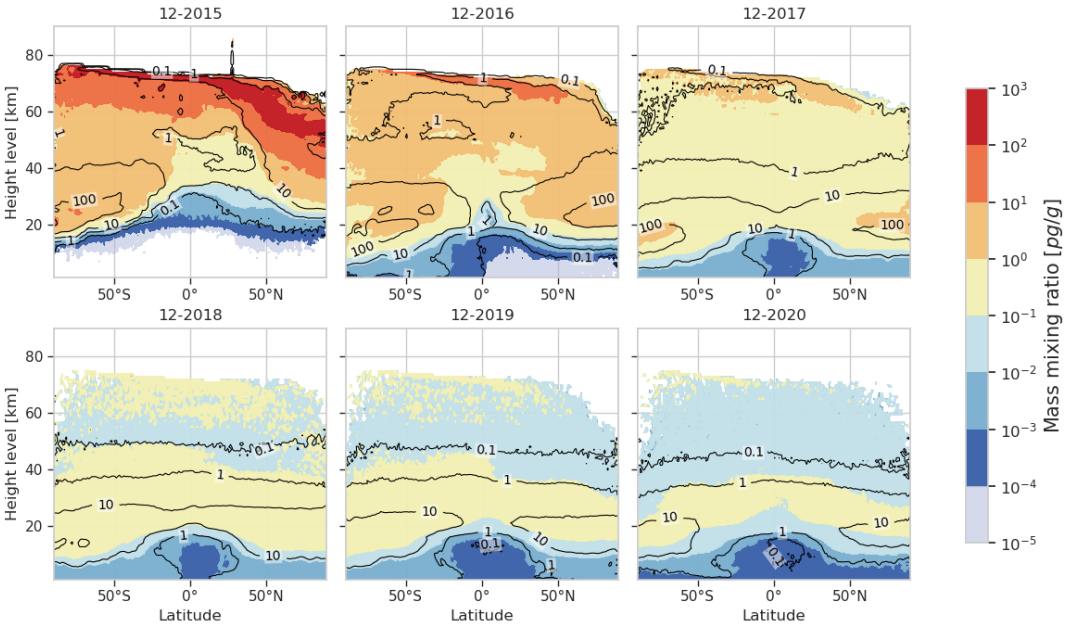

Figure 3.12.: Mass mixing ratio of the vertical distribution of the zonal mean of the alumina particles with a diameter of NO_x in December, for the time period of 2015-2020. Mass concentration is displayed by the black contour lines in pg/m^3.

discussed above, more mass was released in the SH. NO_x sees 55 % of the total deposited mass settled in the SH.

The comparison of wet and dry deposition is displayed in Figure 3.13. Wet deposition is higher than dry deposition in the mid-latitudes, while it equals out around the equator. Higher dry deposition values can be seen on the Great Dividing Range in Australia, New Zealand, Central America, and in some areas in South America and South Africa. Especially in Central America and at the Great Dividing Range, this deviates from the patterns seen in the other species, where these regions are dominated by wet precipitation.

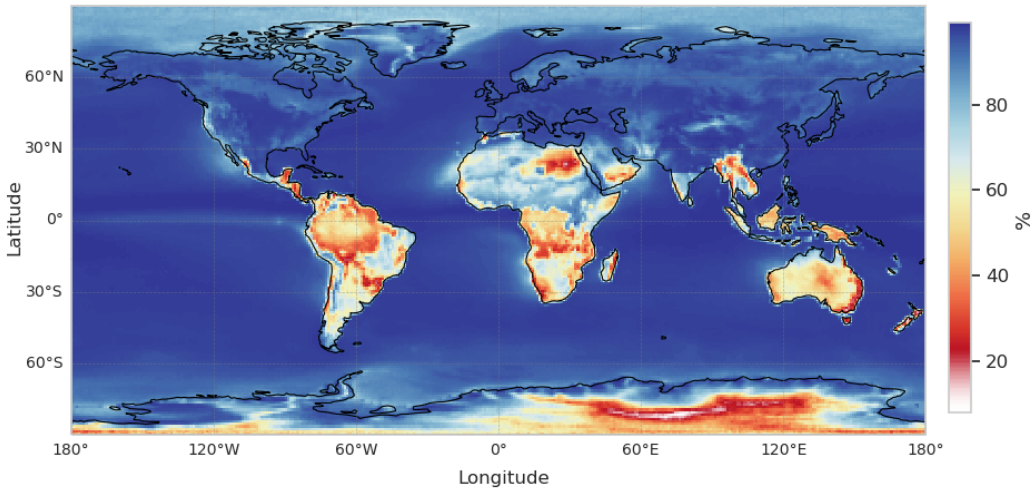

Figure 3.13.: Percentage of wet deposition of the total deposition. Accumulated after 6-years after emission for NO_x.

3.4. Limitations of the present method

For the sake of completeness, the limitations of the here present method will be summarized in this section. Regarding the reentry inventory, a few issues have been arising. First of all, it needs to be noted that there was an offset between the time format of the GMAT model and the TLE messages. The GMAT model expects coordinates in "Mean Equinox Mean Equator" format, whilst the output of the propagated TLE messages is in the "True Equator Mean Equinox" format. The resulting mean absolute error due to this difference is about 16 km for the initial state coordinates, and the mean absolute error in initial state velocity is 0.012 km/s. This error is within the error margin of GMAT model output error, and should therefore not lead to major changes in the satellite reentry trajectories. Of course, going forward, this should be corrected to improve overall accuracy of results. Since the TLE messages have been retrieved from a different dataset than the mass and cross section, pairs were assigned randomly. This, of course, introduces a discrepancy between actual mass values of the object in a TLE message and the here assigned mass and cross section. Going forward this could be solved by matching the TLE messages and mass information by CosparID, an international space objects identification system. The mass information of satellites has been retrieved from DISCOSweb, where multiple categories are present for reentering payloads; in this work, only the "Payload" category was considered. "Payload mission related", "Payload fragmentation debris" and "Payload debris" were not considered when retrieving information on cross section and mass. As explained in section 2.1, these categories only account for a small fraction of reentered mass. The number of reentered objects, on the other hand, is comparable for "Payload fragmentation" and "Payload". With the increasing amount of fragmentation events in Earth's orbit, this should be considered in future work.

Regarding the atmospheric transport modelling, three things should be noted. First of all, alumina particles here were assumed to be spherical. There is very little information about the shape of the alumina aerosols in the burn-up plume of reentering satellites, but different shapes would influence transport behaviour. Since these particles have are in the submicron regime, where shape is not as important, this should not have a significant impact. Secondly, since the releases were made close to the model boundary, the model runs were repeatedly running into the issue that particles were transported to higher altitudes and out of the model boundaries. This led to failure of model runs and restarts were necessary. No inconsistencies were noted due to this, so it should not influence model output results. Finally, NO_x is a reactive gas and undergoes chemical reactions in the atmosphere. These processes are not represented in this modelling approach. The NO_x species can still be interpreted as a precursor for a variety of reactive nitrogen species. Most of the relevant reactions are expected to occur in the stratosphere and troposphere, where conversion into more soluble species HNO_3 and other NO_y species, happens. However, they are in the gas phase and will not behave differently. One should not see NO_x as NO_x but rather as NO_y. The final deposition patterns and lifetime observations can be assumed to be reasonable approximations.

4. Conclusion

This study demonstrates that modelling the emissions of atmospheric satellite reentries with a Lagrangian dispersion model yields valuable insights into their transport pathways. One year of representative emissions from satellite reentries were simulated over a time period of 6-years. These emissions were then accumulated over all years to represent the state of the atmosphere after 6-years of continuous emissions. First deposition signals were observed after 1.5 years for alumina particles with a diameter of 50 nm and 100 nm. After 2 years, significant settling of the alumina tracer could be identified. NO_x showed an atmospheric lifetime of over 2 years, due to its gaseous properties and higher release altitudes. This suggests that species with bigger diameters have a shorter atmospheric lifetime. Gaseous species that are not subject to gravitational settling, here NO_x and the alumina tracer, have a longer atmospheric lifetime. As a result, NO_x and the alumina tracer maintain higher mass mixing ratios over the simulated period. The maximum of the global mean mass concentration for all species is observed at an altitude of 20 km, within the region of the ozone layer. This emphasizes the importance of quantifying the impact of spacecraft reentry emissions, given their potential to affect the ozone layer. The large-scale transport of these emissions could be identified. Emissions are mainly released in the Mesosphere and Upper Stratosphere, from where they sink into lower atmospheric layers. The main transport is dominated by the Brewer-Dobson circulation, transporting emissions towards the winter poles. At the poles, the highest mass mixing ratios and concentration are found. The tropics showed comparatively lower mass mixing ratios than other regions. The main region of deposition was found to be the mid-latitudes. This proves the hypothesised transport pathways: transport from the equator towards the poles, where air descends in dry intrusions from the stratosphere into the mid-latitude troposphere, where mainly wet deposition processes lead to scavenging out of the atmosphere. Further, it was found that filamentous structures develop in the emission fields. These structures suggest that atmospheric transport processes lead to strong spatial heterogeneity in the distribution of the emitted material. The formation of such filamentary structures highlights the importance of accurately resolving transport pathways when analysing the dispersion of space-debris emissions. Evaluating the impact of the location of reentry shows that the highest mmr are seen at the emission region. Polar releases are distributed on a global scale, but result in lower mmr in the tropics. Emissions in the tropics and mid-latitudes are transported towards the winter pole in each hemisphere. However, concentrations remain slightly higher in the hemisphere where more mid-latitude reentries occur. Emissions follow the main transport pathways dominated by the BDC, showing that the month of reentry, as well as reentry location, are the dominating factors for the subsequent transport.

Whilst this study provided valuable insight into these processes, further research is warrant. Of particular interest is the behaviour of particles with even smaller than 50 nm diameter; the sensitivity study could therefore be extended to particles with diameter of 10 nm to 1 nm.

This would improve the understanding of smaller particles and bridge the gap between the alumina tracer and the 50 nm particles, between which differing lifetimes have been observed. Since not all mass had been deposited by the end of the modelled period, it would be of interest to extend simulations by an extra year, to see how long it takes for all emissions to be fully deposited. Alumina and NO_x are not the only species produced during satellite reentry processes; it is of interest to investigate the behaviour of other climate relevant emissions. Moreover, a substantial part of emissions in the space industry are due to rocket launches. It is necessary to include the emissions from rocket launches, too, since their emission profile differs to that of satellites, particularly due to their release at lower altitudes.

Bibliography

Bakels, L. et al. (2024). “FLEXPART version 11: improved accuracy, efficiency, and flexibility”. *Geoscientific Model Development* 17.21, pp. 7595–7627. https://doi.org/10.5194/gmd-17-7595-2024.

Barker, C. R., E. A. Marais and J. C. McDowell (2024). “Global 3D rocket launch and re-entry air pollutant and CO2 emissions at the onset of the megaconstellation era”. *Scientific Data* 11.1, p. 1079. https://doi.org/10.1038/s41597-024-03910-z.

Bekki, S. et al. (2021). “Environmental impacts of atmospheric emissions from spacecraft re-entry demise”. *ESA Clean-Space Industrial Days*. https://indico.esa.int/event/321/contributions/6403/attachments/4335/6538/esa-csid-21-bekki.pdf.

Bernlochner, S., M. Nützel, B. Mayer, A. Schmidt and C. Maloney (2026). *Sensitivity analysis of radiative effects of alumina particles from spacecraft re-entries*. Tech. rep. EGU26-7078. Copernicus Meetings. https://doi.org/10.5194/egusphere-egu26-7078.

Botelho, R. and A. Xavier (2019). “A Unified Satellite Taxonomy Proposal Based on Mass and Size”. *Advances in Aerospace Science and Technology* 04, pp. 57–73. https://doi.org/10.4236/aast.2019.44005.

Butchart, N. (2014). “The Brewer-Dobson circulation”. *Reviews of Geophysics* 52.2, pp. 157–184. https://doi.org/10.1002/2013RG000448.

Carrillo-Sánchez, J. D. et al. (2020). “Cosmic dust fluxes in the atmospheres of Earth, Mars, and Venus”. *Icarus* 335, p. 113395. https://doi.org/10.1016/j.icarus.2019.113395.

Danilin, M. Y., M. K. W. Ko and D. K. Weisenstein (2001). “Global implications of ozone loss in a space shuttle wake”. *Journal of Geophysical Research: Atmospheres* 106.D4, pp. 3591–3601. https://doi.org/10.1029/2000JD900632.

Deshler, T. (2008). “A review of global stratospheric aerosol: Measurements, importance, life cycle, and local stratospheric aerosol”. *Atmospheric Research*. 17th International Conference on Nucleation and Atmospheric Aerosols 90.2, pp. 223–232. https://doi.org/10.1016/j.atmosres.2008.03.016.

Dresselhaus, M., G. Dresselhaus, S. Cronin and A. Gomes Souza Filho (2018). *Solid State Properties*. Graduate Texts in Physics. Berlin, Heidelberg: Springer. https://doi.org/10.1007/978-3-662-55922-2.

Eastham, S. D. and D. J. Jacob (2016). *Limits on the ability of global Eulerian models to resolveintercontinental transport of chemical plumes*. https://doi.org/10.5194/acp-2016-943.

ESA (2024). “Space Environment Report”. *2024*.

– (2025a). *Database and Information System Characterising Objects in Space (DISCOS)*. https://discosweb.esoc.esa.int/ (visited on 28/02/2026).

– (2025b). “Space Environment Report”. *2025*.

Fisher, M., A. O'Neill and R. Sutton (1993). "Rapid descent of mesospheric air into the stratospheric polar vortex". *Geophysical Research Letters* 20.12, pp. 1267–1270. https://doi.org/10.1029/93GL01104.

Greene, B. R. and C. M. Sanchez (2019). "Demisability of GFRP and CFRP Components of Reentering Orbital Debris: Phase I Test Results". El Segundo, CA. https://ntrs.nasa.gov/citations/20190025208 (visited on 30/03/2025).

Hersbach, H. et al. (2020). "The ERA5 global reanalysis". *Quarterly Journal of the Royal Meteorological Society* 146.730, pp. 1999–2049. https://doi.org/10.1002/qj.3803.

Hervig, M. E. et al. (2022). "Decadal and Annual Variations in Meteoric Flux From Ulysses, Wind, and SOFIE Observations". *Journal of Geophysical Research: Space Physics* 127.10, e2022JA030749. https://doi.org/10.1029/2022JA030749.

Hughes, S. (2007). *General Mission Analysis Tool (GMAT) Mathematical Specifications*. https://ntrs.nasa.gov/citations/20080031744 (visited on 21/11/2025).

Jackman, C., D. Considine and E. Fleming (1998). "A global modeling study of solid rocket aluminum oxide emission effects on stratospheric ozone". *Geophysical Research Letters* 25.6, pp. 907–910. https://doi.org/10.1029/98GL00403.

Jacob, D. J. (1999). *Introduction to atmospheric chemistry*. Princeton, N.J. : Princeton University Press. http://archive.org/details/introductiontoat0000jaco (visited on 16/04/2026).

Jah, M., H. Steven, M. Wilkins and T. Kelecy (2009). "THE GENERAL MISSION ANALYSIS TOOL (GMAT): A NEW RESOURCE FOR SUPPORTING DEBRIS ORBIT DETERMINATION, TRACKING AND ANALYSIS". *Proceedings of the 5th European Conference on Space Debris*. ESA SP-672. Darmstadt, Germany.

Jain, A. K. (2023). "On the Atmospheric Saliency of Space Debris Reentries: Estimating Distribution, Lifetime and Radiative Forcing of Reentry-Ablated Alumina". Thesis. Massachusetts Institute of Technology. https://dspace.mit.edu/handle/1721.1/151443 (visited on 03/04/2025).

Katharopoulos, I. (2026). *Advances in Inverse Modelling for the Estimation of Greenhouse Gas Emissions*. https://www.research-collection.ethz.ch/entities/publication/d040c385-6918-4384-bf78-1de1df398a9b (visited on 11/04/2026).

Kelley, R. L., N. M. Hill, W. C. Rochelle, N. L. Johnson and T. Lips (2010). "Comparison of ORSAT and SCARAB Reentry Analysis Tools for a Generic Satellite Test Case". Bremen. https://ntrs.nasa.gov/citations/20100005304 (visited on 01/04/2025).

Kelso, T. (2026). *CelesTrak: "FAQs: Two-Line Element Set Format"*. https://celestrak.org/columns/v04n03/ (visited on 10/04/2026).

Klinkrad, H. and B. Fritsche (1998). "Orbit and attitude perturbations due to aerodynamics and radiation pressure". *ESA workshop on space weather, ESTEC, Noordwijk, Netherlands*.

Krebs, G. (2026). *Starlink Block v2-Mini*. https://space.skyrocket.de/doc_sdat/starlink-v2-mini.htm (visited on 01/04/2026).

Larson, E. J. L. et al. (2017). "Global atmospheric response to emissions from a proposed reusable space launch system". *Earth's Future* 5.1, pp. 37–48. https://doi.org/10.1002/2016EF000399.

Maloney, C. M., R. W. Portmann, M. N. Ross and K. H. Rosenlof (2025). "Investigating the Potential Atmospheric Accumulation and Radiative Impact of the Coming Increase in Satellite Reentry Frequency". *Journal of Geophysical Research: Atmospheres* 130.6, e2024JD042442. https://doi.org/10.1029/2024JD042442.

Matori, K., L. Wah, M. Hashim, I. Ismail and M. Zaid (2012). "Phase Transformations of -Alumina Made from Waste Aluminum via a Precipitation Technique". *International Journal of Molecular Sciences* 13.12, pp. 16812–16821. https://doi.org/10.3390/ijms131216812.

McDowell, J. C. (2025). *GCAT: General Catalog of Artificial Space Objects*. https://www.planet4589.org/space/.

Murphy, D. M. et al. (2023). "Metals from spacecraft reentry in stratospheric aerosol particles". *Proceedings of the National Academy of Sciences* 120.43. https://doi.org/10.1073/pnas.2313374120.

Oliveira, D. M., E. Zesta and K. Garcia-Sage (2025). "Tracking reentries of Starlink satellites during the rising phase of solar cycle 25". *Frontiers in Astronomy and Space Sciences* 12. https://doi.org/10.3389/fspas.2025.1572313.

Ostrom, C. et al. (2019). "Operational and technical updates to the object reentry survival analysis tool". *International Orbital Debris Conference (IOC)*. JSC-E-DAA-TN73668.

Pardini, C. and L. Anselmo (2024). "The risk of casualties from the uncontrolled re-entry of spacecraft and orbital stages". *Journal of Space Safety Engineering* 11.2, pp. 181–191. https://doi.org/10.1016/j.jsse.2024.02.002.

Park, S.-H. and G. Park (2017). "Reentry trajectory and survivability estimation of small space debris with catalytic recombination". *Advances in Space Research* 60.5, pp. 893–906. https://doi.org/10.1016/j.asr.2017.05.004.

Picone, J. M., A. E. Hedin, D. P. Drob and A. C. Aikin (2002). "NRLMSISE-00 empirical model of the atmosphere: Statistical comparisons and scientific issues". *Journal of Geophysical Research: Space Physics* 107.A12. https://doi.org/10.1029/2002JA009430.

Pines, S. (1973). "Uniform Representation of the Gravitational Potential and its Derivatives". *AIAA Journal* 11, pp. 1508–1511. https://doi.org/10.2514/3.50619.

Pisso, I. et al. (2019). "The Lagrangian particle dispersion model FLEXPART version 10.4". *Geoscientific Model Development* 12.12, pp. 4955–4997. https://doi.org/10.5194/gmd-12-4955-2019.

Plumb, R. A. et al. (2002). "Global tracer modeling during SOLVE: High-latitude descent and mixing". *Journal of Geophysical Research: Atmospheres* 107.D5. https://doi.org/10.1029/2001JD001023.

Raschka, S., Y. Liu, V. Mirjalili and D. Dzhulgakov (2022). *Machine Learning with PyTorch and Scikit-Learn: Develop machine learning and deep learning models with Python*. Birmingham: Packt Publishing.

Rhodes, B. (2019). "Skyfield: High precision research-grade positions for planets and Earth satellites generator". *Astrophysics Source Code Library*, ascl:1907.024. https://ui.adsabs.harvard.edu/abs/2019ascl.soft07024R (visited on 01/04/2026).

– (2025). *SGP4 Python library*. https://github.com/brandon-rhodes/python-sgp4.

Ross, M. N. and P. M. Sheaffer (2014). "Radiative forcing caused by rocket engine emissions". *Earth's Future* 2.4, pp. 177–196. https://doi.org/10.1002/2013EF000160.

Ryan, R. G., E. A. Marais, C. J. Balhatchet and S. D. Eastham (2022). "Impact of Rocket Launch and Space Debris Air Pollutant Emissions on Stratospheric Ozone and Global Climate". *Earth's Future* 10.6, e2021EF002612. https://doi.org/10.1029/2021EF002612.

Schulz, L. et al. (2025). *Space waste: An update of the anthropogenic matter injection into Earth atmosphere*. https://doi.org/10.48550/arXiv.2510.21328.

Seinfeld, J. H. and S. N. Pandis (2016). *Atmospheric chemistry and physics from air pollution to climate change*. Third edition. Hoboken, New Jersey: John Wiley & Sons. https://ebookcentral.proquest.com/lib/ed/detail.action?docID=4462549.

Space-Track.org (2026). https://www.space-track.org/ (visited on 25/05/2026).

Stohl, A., C. Forster, A. Frank, P. Seibert and G. Wotawa (2005). "Technical note: The Lagrangian particle dispersion model FLEXPART version 6.2". *Atmos. Chem. Phys.*

Tatsii, D. (2025). "Atmospheric transport of microplastics". https://doi.org/10.25365/thesis.78247.

Tritscher, I. et al. (2021). "Polar Stratospheric Clouds: Satellite Observations, Processes, and Role in Ozone Depletion". *Reviews of Geophysics* 59.2, e2020RG000702. https://doi.org/10.1029/2020RG000702.

United States Government Accountability Office (2022). *Large Constellation of Satellites: Mitigating Environmental and Other Effects*. Tech. rep. U.S.Government Printing Office.

Vallado, D. A. and P. J. Cefola (2012). "TWO-LINE ELEMENT SETS – PRACTICE AND USE". *63rd International Astronautical Congress*.

Vallado, D. A., P. Crawford and R. Hujsak (2006). *Revisiting Spacetrack Report #3: Rev 3*. https://celestrak.org/publications/AIAA/2006-6753/.

Wang, X. et al. (2024). "Estimates of Spherical Satellite Drag Coefficients in the Upper Thermosphere During Different Geomagnetic Conditions". *Space Weather* 22.11, e2024SW003974. https://doi.org/10.1029/2024SW003974.

Xu (2024). *Effects of Aluminum/Carbon and Morphology on Optical Characteristics and Radiative Forcing of Alumina Clusters Emitted by Solid Rockets in the Stratosphere - ProQuest*. https://www.proquest.com/openview/1bf3f47065324e5e2a1b66548326b256/1?cbl=2032431&pq-origsite=gscholar (visited on 22/05/2025).

Ziniu, W., R. Hu, Q. Xi, W. Xiang and W. Zhe (2011). "Space Debris Reentry Analysis Methods and Tools". *Chinese Journal of Aeronautics* 24, pp. 387–395. https://doi.org/10.1016/S1000-9361(11)60046-0.

A. Appendix

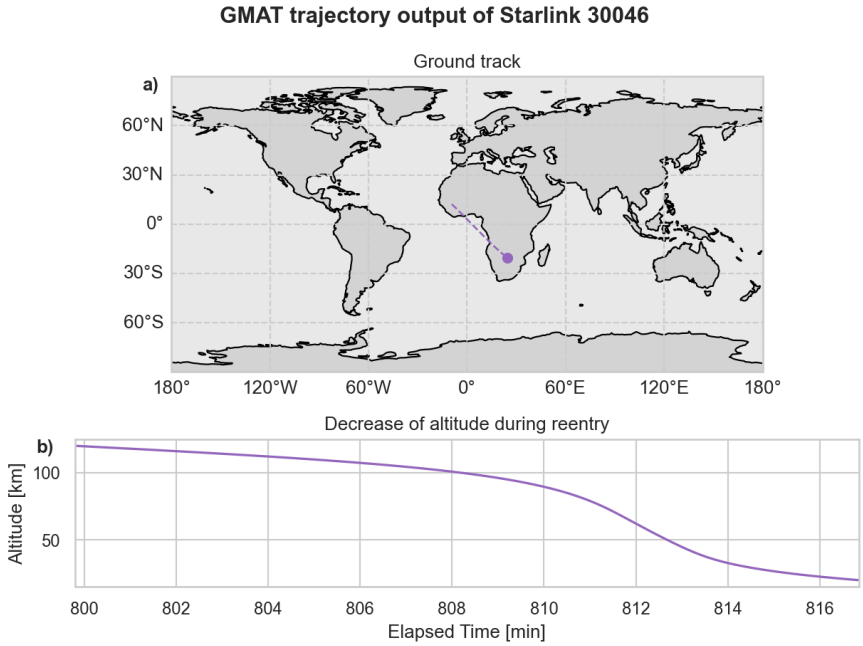

Figure A.1.: Reentry trajectory of the Starlink 30046 satellite, modelled with GMAT. The circle marks the end point of the trajectory, at an altitude of 20 km. Plot a) shows the ground track, and b) the altitude by elapsed time starting from 120 km. The x-axis starts at 800 min, since the trajectory needed to be propagated starting from the last sent TLE message, which was at a higher altitude.

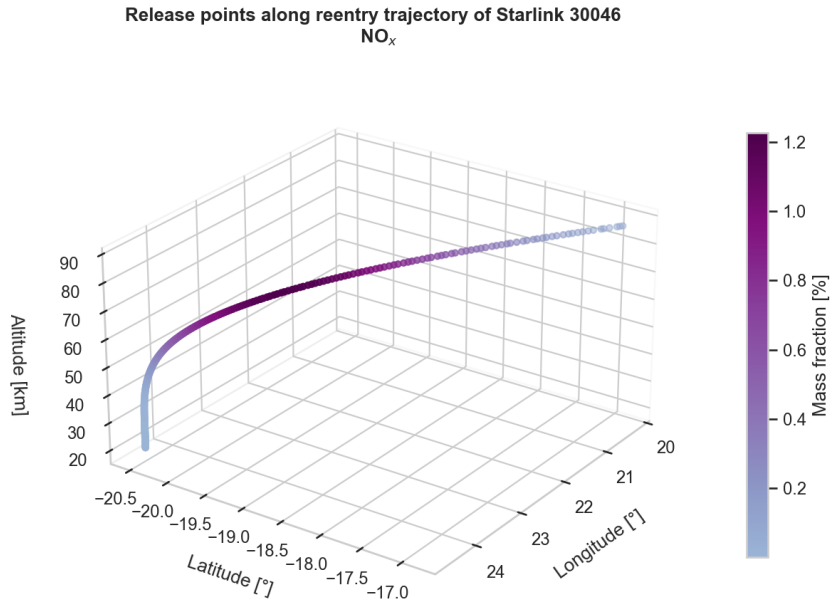

Figure A.2.: Example of the injected NO_x mass as a fraction of satellite mass, as a function of latitude, longitude and altitude, for the example of Starlink satellite 30046. Emissions are discretized to 397 release points at which mass is injected into the atmosphere for the purpose of atmospheric transport modelling.

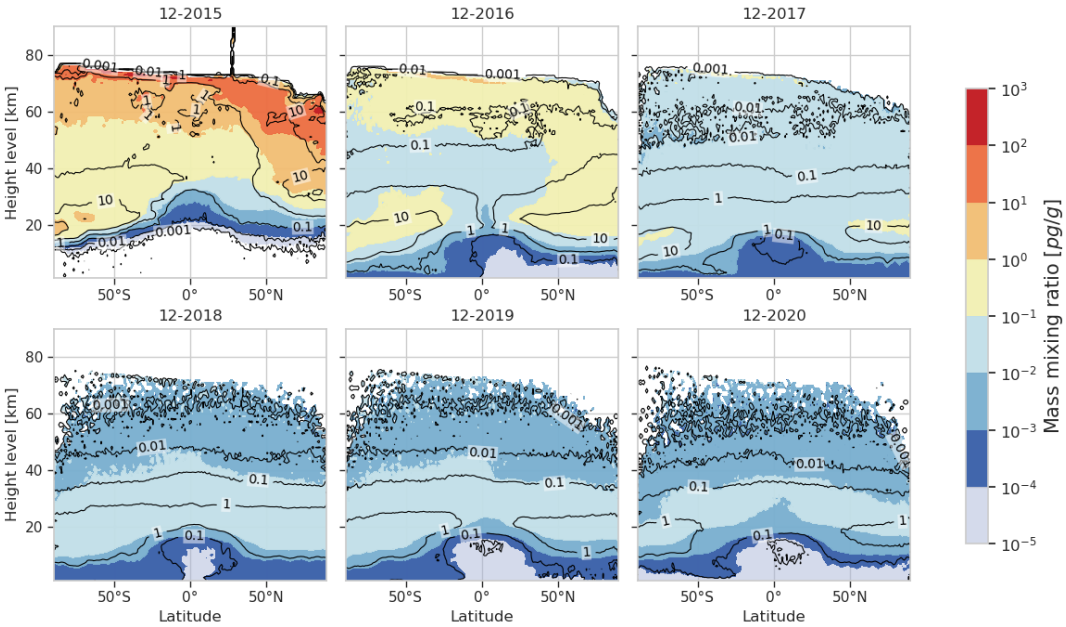

Figure A.3.: Mass mixing of the vertical distribution of the zonal mean of the alumina tracer particles in December of each year for the time period of 2015-2020. Mass concentration is displayed by the black contour lines in pg/m^3.

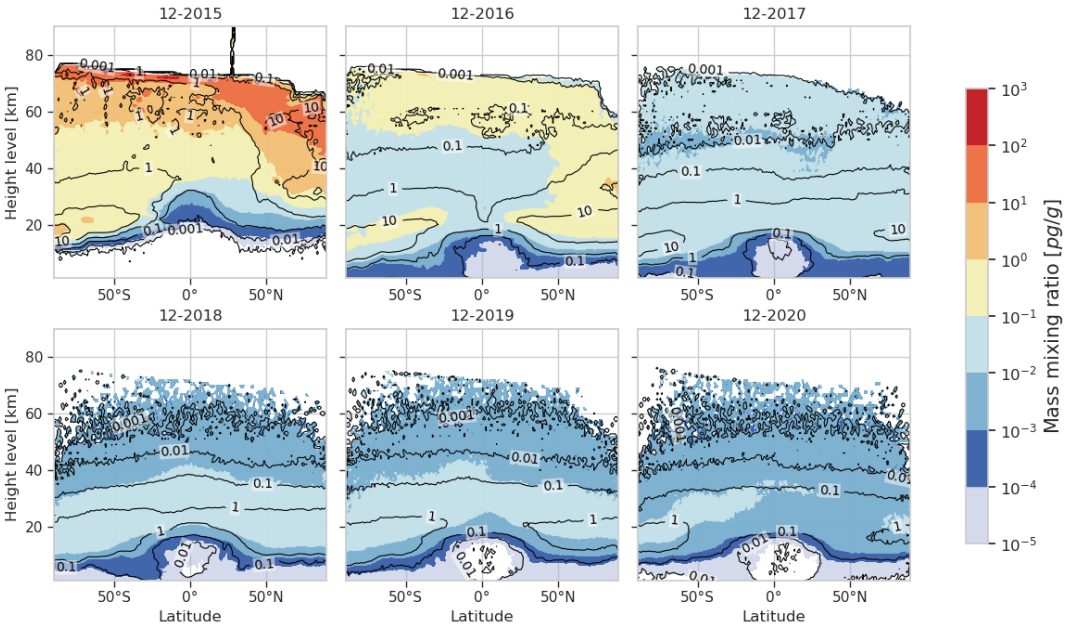

Figure A.4.: Mass mixing ratio of the vertical distribution of the zonal mean of the alumina particles with a diameter of 100 nm in December of each year, for the time period of 2015-2020. Mass concentration is displayed by the black contour lines in pg/m^3.

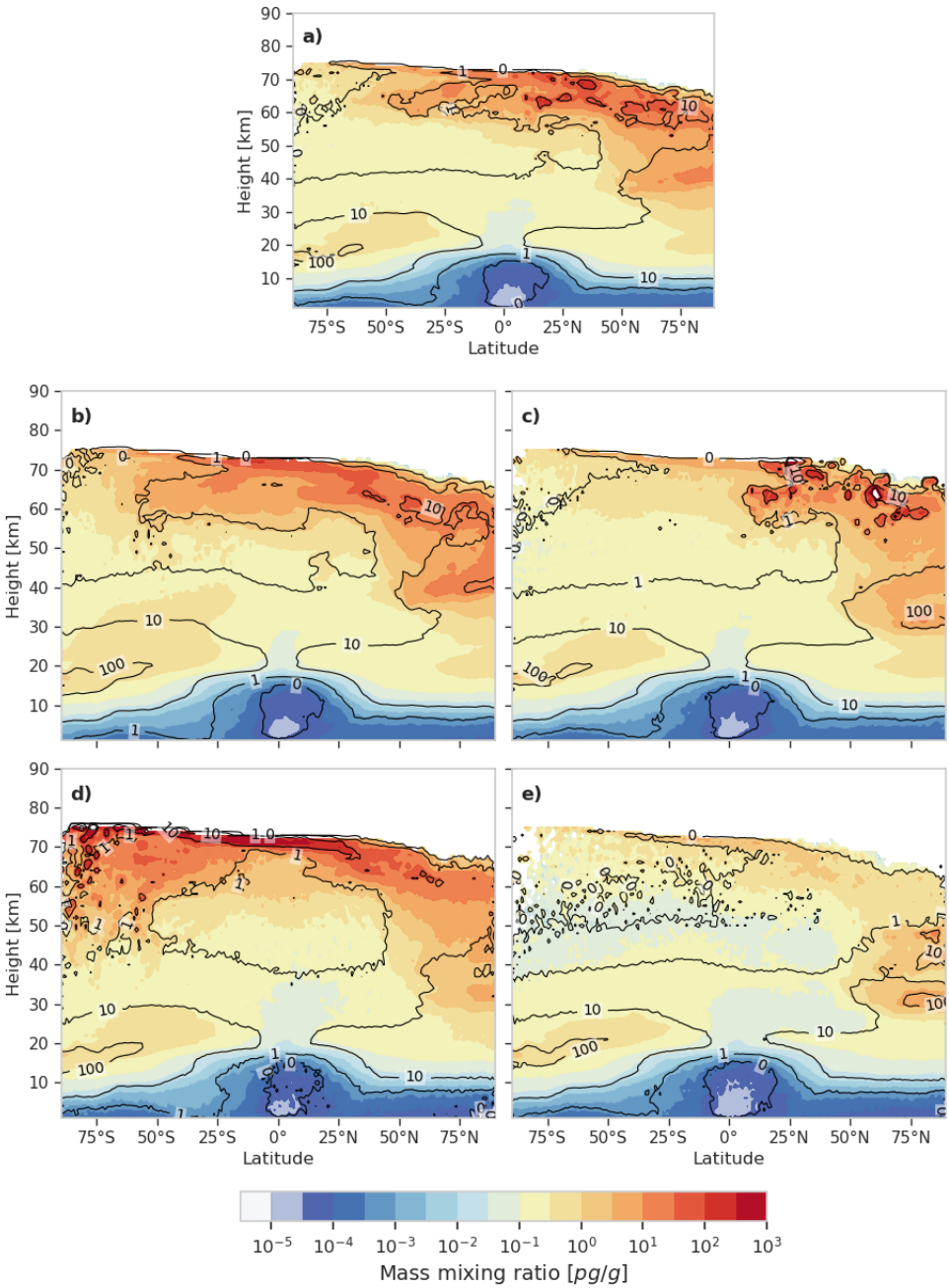

Figure A.5.: Six-year sum of the zonal-mean mass mixing ratio of alumina particles with a diameter of 50 nm, for January. For each subplot, only reentries within the indicated region are considered: (a) tropics, (b) subtropics and mid-latitudes in the Southern Hemisphere, (c) subtropics and mid-latitudes in the Northern Hemisphere, (d) polar region of the Southern Hemisphere, and (e) polar region of the Northern Hemisphere. Each region is scaled by the fraction of total mass relative to the emitted mass in the respective region. Mass concentration is displayed by the black contour lines in pg/m^3.

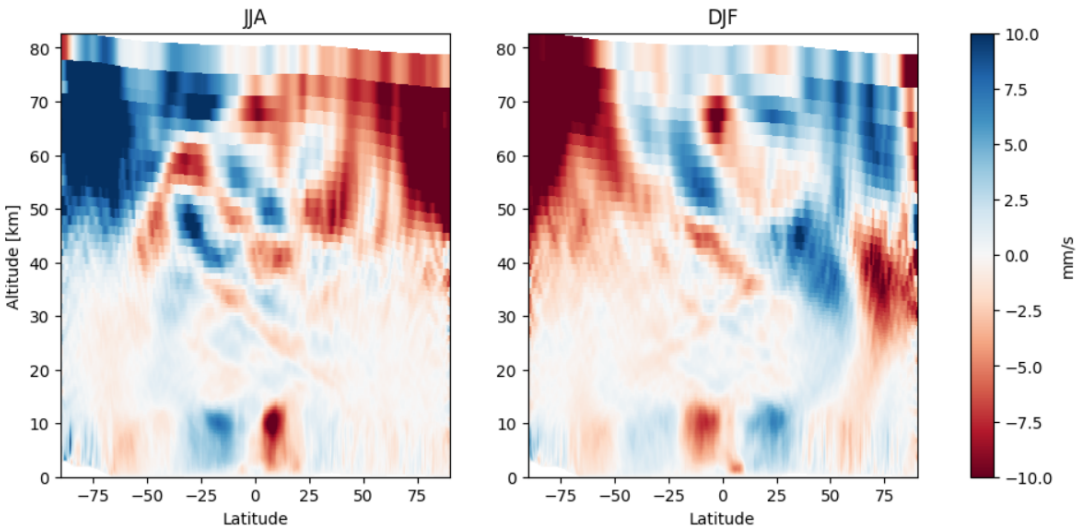

Figure A.6.: Vertical velocity from ERA5 as mean of June, July and August is shown in the left panel, and December, January and February in the right panel. A negative sign indicates upward motion, since this parameter is based on the Eta-coordinate system, where pressure decreases with increasing altitude.

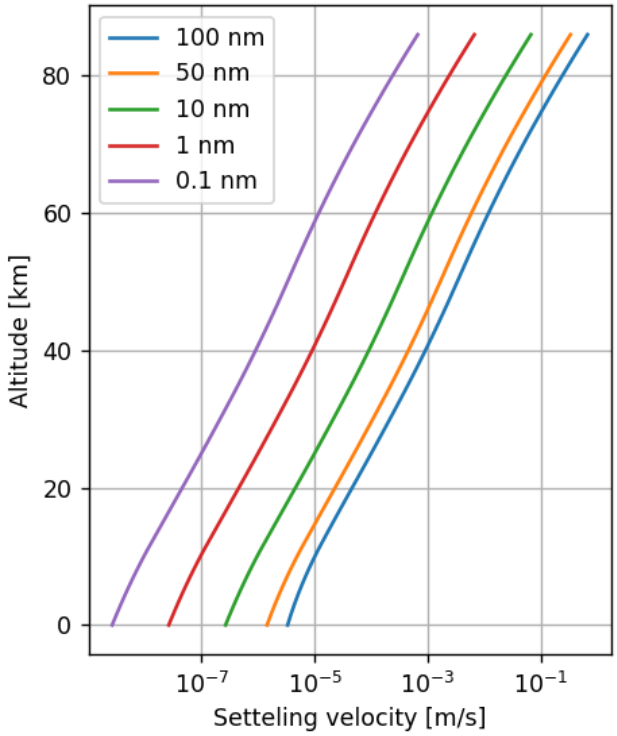

Figure A.7.: Settling velocity for spherical alumina aerosols with a density of ρ_p = 3950 kg/m^3.

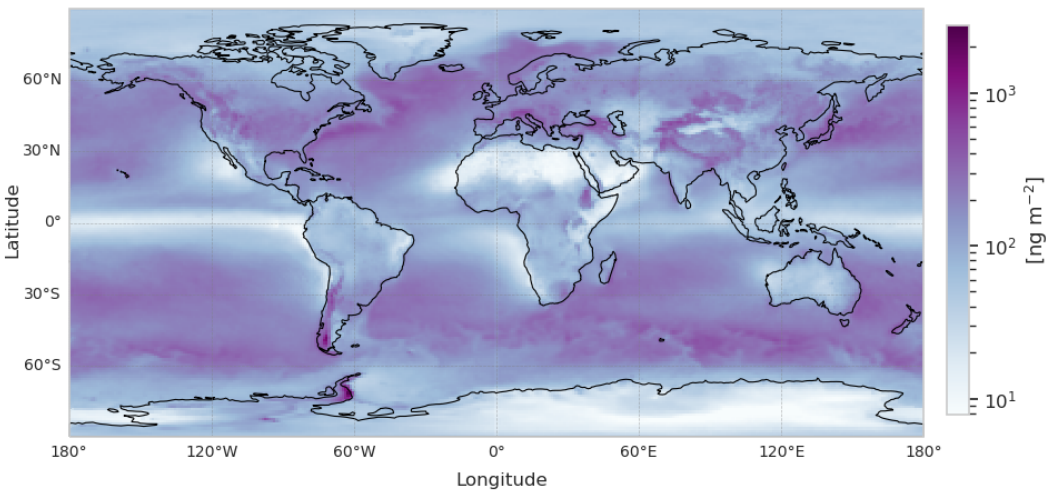

Figure A.8.: Spatial distribution of deposited mass in ng/m^2 of particles with a diameter of 100 nm at the end of the modelled period

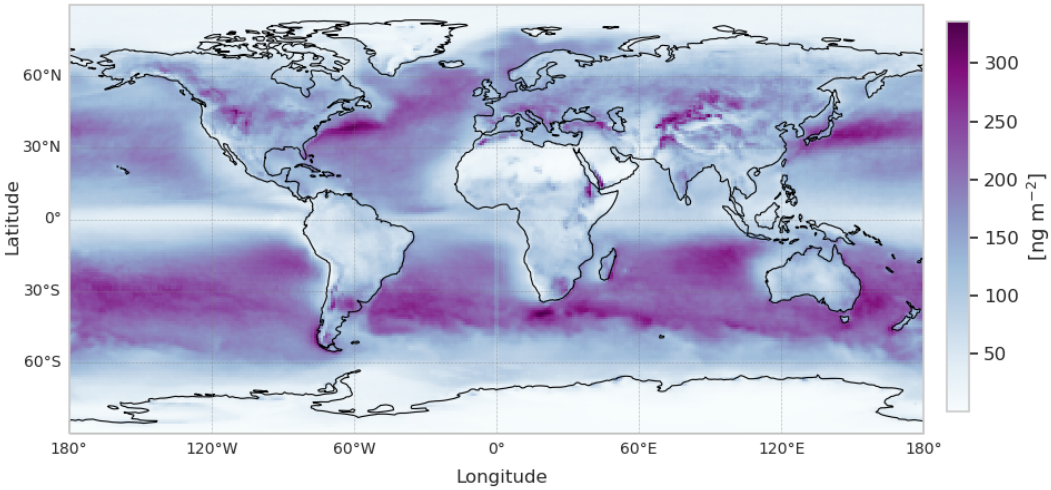

Figure A.9.: Spatial distribution of deposited mass in ng/m^2 of alumina tracer particles at the end of the modelled period.

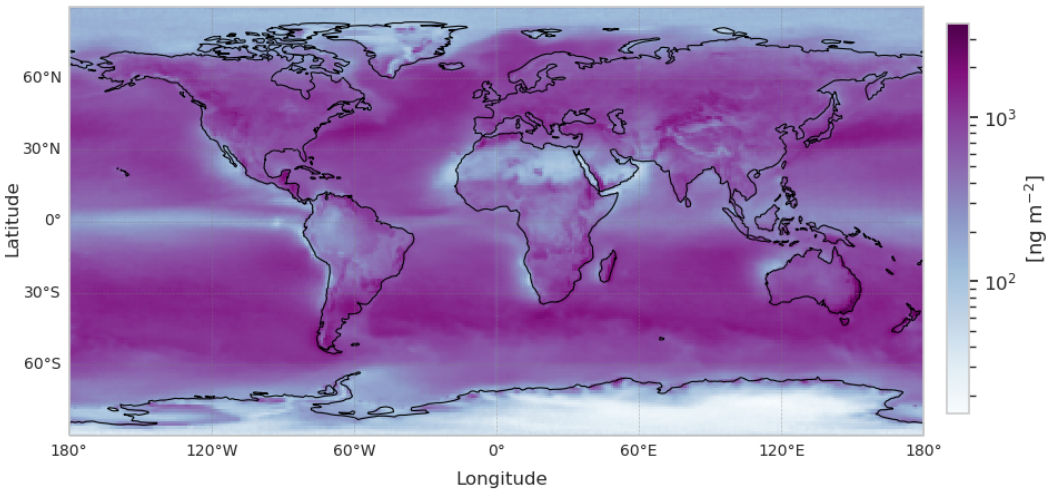

Figure A.10.: Spatial distribution of deposited mass in ng/m^2 of NO_x at the end of the modelled period.

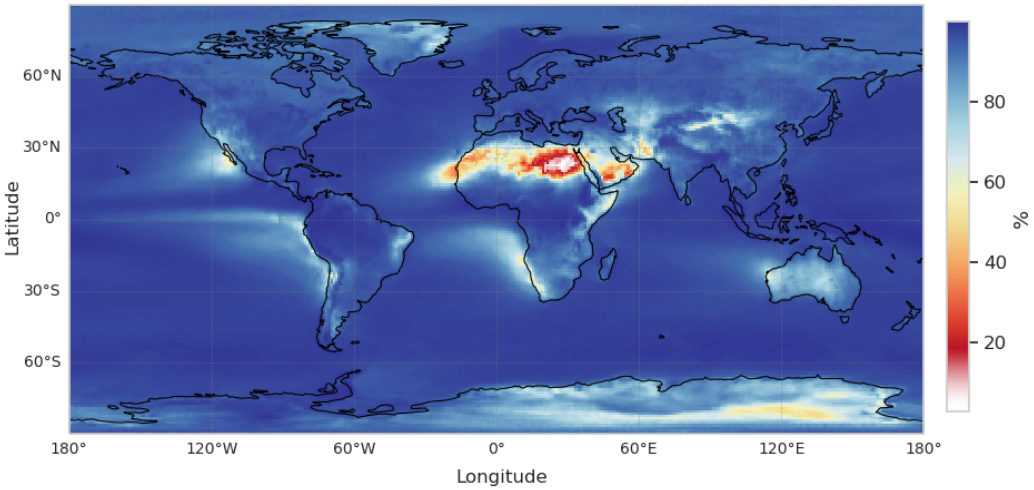

Figure A.11.: Percentage of wet deposition of the total deposition. Accumulated after 5-years after emission of particles with a diameter of 100 nm.

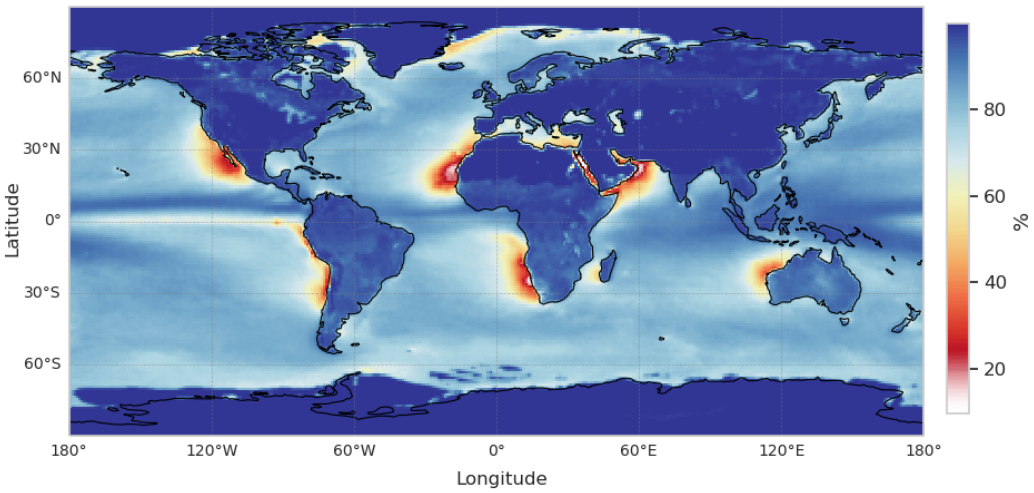

Figure A.12.: Percentage of wet deposition of the total deposition. Accumulated after 5-years after emission of particles, the alumina tracer.